

# Design of Active Defects in Semiconductors: 3D Electron Diffraction Revealed Novel Organometallic Lead Bromide Phases Containing Ferrocene as Redox Switches

Nicole Fillafer, Henning Kuper, Andreas Schaate, Sonja Locmelis, Joerg August Becker, Yaşar Krysiak,\* and Sebastian Polarz\*

Once the optical, electronic, or photocatalytic properties of a semiconductor are set by adjusting composition, crystal phase, and morphology, one cannot change them anymore, respectively, on demand. Materials enabling post-synthetic and reversible switching of features such as absorption coefficient, bandgap, or charge carrier dynamics are highly desired. Hybrid perovskites facilitate exceptional possibilities for progress in the field of smart semiconductors because active organic molecules become an integral constituent of the crystalline structure. This paper reports the integration of ferrocene ligands into semiconducting 2D phases based on lead bromide. The complex crystal structures of the resulting, novel ferrovskite ( $\approx$  ferrocene perovskite) phases are determined by 3D electron diffraction. The ferrocene ligands exhibit strong structure-directing effects on the 2D hybrid phases, which is why the formation of exotic types of face- and edge-sharing lead bromide octahedra is observed. The bandgap of the materials ranges from 3.06 up to 3.51 eV, depending on the connectivity of the octahedra. By deploying the redox features of ferrocene, one can create defect states or even a defect band leading to control over the direction of exciton migration and energy transport in the semiconductor, enabling fluorescence via indirect to direct gap transition.

crystal structure, or nanostructure. However, it is quite common that the obtained materials have more or less strongly changed or even unexpected properties because of the presence of defects. Although defects are enthalpically unfavorable, they occur due to the contribution of entropy to free energy. Their frequent statistical occurrence makes them difficult to localize and to quantify and cannot yet be used to influence the properties of a material by purpose. Ideally, a defect can be switched on and off as desired. Substitutional point defects are of utmost importance in semiconductor materials as they have a direct consequence on doping, the number and type of mobile charge carriers, and bandgap engineering in general.<sup>[1,2]</sup> Once a heteroatom is introduced at a defined concentration into classical semiconductors such as Si, II–VI (e.g., ZnO), or III–V (e.g., GaN) compounds, the properties associated to the degree of doping are set.

Imagine a material which ideally could change fast, reversibly and on demand

## 1. Introduction


Research in materials chemistry aims to control the properties of a material by precisely adjusting parameters such as composition,

from a doped to an undoped (= defect-free) state. The development of such responsive semiconductor materials stands at its very beginning. It is obviously hard to create the described type of active defects in traditional semiconductor solids. However, recently major scientific attention was devoted to a new class, the so-called hybrid perovskites materials. Easy processability and unique properties brought hybrid organic–inorganic perovskites to the forefront of semiconductor research.<sup>[3]</sup> In the last decade, they emerged as a genuine alternative to silicon, especially in photovoltaic applications.<sup>[4,5]</sup> But the ultralow cost materials are not only used in photovoltaics. Exceptional properties such as long-range electron and hole transport lengths,<sup>[6]</sup> high absorption coefficients,<sup>[7]</sup> a variably bandgap,<sup>[8,9]</sup> and high photoluminescence (PL) quantum yields<sup>[10]</sup> promoted the development of optoelectronic devices as transistors, light-emitting diodes, and photodetectors.<sup>[11]</sup> One reason for the wide range of applications is the possibility to adjust the electro-optical properties by specific compositions (e.g., anion exchange) and dopants (e.g., Bi<sup>3+</sup>, Au<sup>3+</sup>, In<sup>3+</sup>, Mn<sup>2+</sup>).<sup>[12–15]</sup>

One of the most interesting and most important features of hybrid perovskites is that larger and functional organic molecules can be included as integral parts of the crystal lattice. A

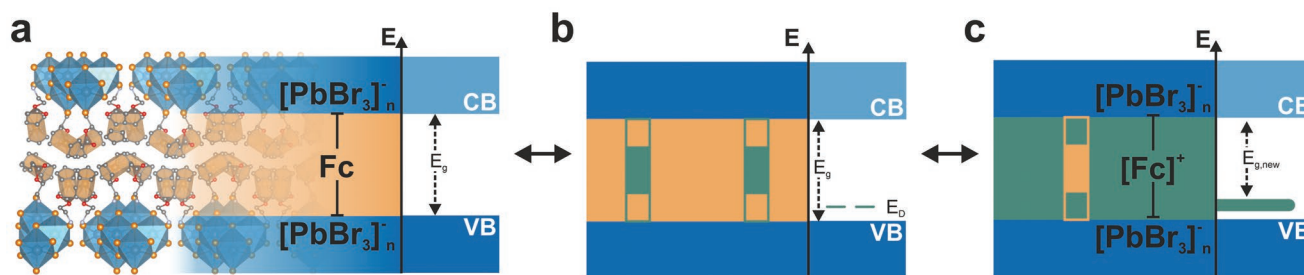
N. Fillafer, A. Schaate, S. Locmelis, Y. Krysiak, S. Polarz  
Institute of Inorganic Chemistry  
Leibniz University of Hannover  
Callinstraße 9, 30167 Hannover, Germany  
E-mail: yasar.krysiak@aca.uni-hannover.de;  
sebastian.polarz@aca.uni-hannover.de

H. Kuper, J. A. Becker  
Institute of Physical Chemistry  
Leibniz University of Hannover  
Callinstraße 3-3a, 30167 Hannover, Germany

 The ORCID identification number(s) for the author(s) of this article can be found under <https://doi.org/10.1002/adfm.202201126>.

© 2022 The Authors. Advanced Functional Materials published by Wiley-VCH GmbH. This is an open access article under the terms of the Creative Commons Attribution-NonCommercial License, which permits use, distribution and reproduction in any medium, provided the original work is properly cited and is not used for commercial purposes.

DOI: 10.1002/adfm.202201126



**Scheme 1.** a) Representation of a semiconductor crystal with integrated Fc and the bandgap scheme in the intrinsic state, b) with a small amount of oxidized Fc-ligands causing defect states in the bandgap  $E_D$ , and c) with a high amount of oxidized Fc-ligands causing a new defect band in the bandgap.

consequence is the reduction of the dimensionality of the inorganic lead halide network, respectively, the formation of layered structures such as the Ruddlesden–Popper phases.<sup>[16,17]</sup> With organic cations exceeding the space given by the perovskite structure, layered hybrid perovskites (LHPs) are obtained. The structural diversity of LHPs depends strongly on the organic cation that serves as a template, but also the choice of halide ( $\text{Cl}^-$ ,  $\text{Br}^-$ ,  $\text{I}^-$ ).<sup>[18–20]</sup> Sterically demanding cations or cations with a strong templating effect lead to more complex metal halide structures compared to the classic arrangement of lead halide octahedra.<sup>[21]</sup> Other than in perovskite-related structures, these phases feature not only corner-, but also edge- and face-sharing octahedra. These structures led to the so-called *perovskitoids*, perovskite-like structures, which show enhanced stability and are therefore highly attractive for photovoltaic applications.<sup>[22–24]</sup> Reported are 1D *perovskitoids*,<sup>[25]</sup> but as well 2D and 3D structures are already available.<sup>[26–28]</sup> The electronic structure of the conduction and valence band is influenced by both constituents, the inorganic and the organic.<sup>[19,29]</sup> Due to the confinement of the charge carriers, the inorganic layers behave like quantum wells.<sup>[30]</sup> The role of the organic ligands is equally important.<sup>[31]</sup> Conductive,<sup>[30,32]</sup> polymerizable,<sup>[33]</sup> and photoactive<sup>[34]</sup> organic functionalities have already been incorporated into LHPs.

It has not yet been possible to incorporate a ligand with which the electro-optical properties, e.g., the bandgap or photoluminescence properties can *actively* be controlled. One might think that photoactive ligands are most suitable for this purpose, but electronically active transition states are quenched by the semiconductor.<sup>[34]</sup> Zhang et al. presented an important paper on 1D lead halide phase containing ferrocene (Fc) with exceptional piezoelectric properties.<sup>[35]</sup> The paper envisions that the combination of organometallic compounds with the structurally diverse class of hybrid perovskites opens up novel possibilities. However, one of the most important functionalities of Fc, its unique redox properties, was not addressed. This is surprising because Fc has proven to be a valuable building block in many other areas of material science research. Fc has already been used in battery materials, polymers<sup>[36]</sup> and metal–organic frameworks (MOFs) to artificially create conductivity.<sup>[37]</sup> In MOFs, which usually have localized electronic stages, charge transfer between the surface bound Fc-ligands could be observed during the oxidation.<sup>[38]</sup> The fast redox reaction and adjustable optical and electronic properties<sup>[39]</sup> make it a perfect candidate as an electro-optically active ligand.

We report here the targeted synthesis of novel layered hybrid lead halide phases containing layers of tailor-made ferrocene (Fc) derivatives (**Scheme 1**) which allow bandgap tuning by

the incorporation of active defects. The underlying idea is that doping of the perovskite material occurs when the number of oxidized ferrocene ( $\text{Fc}^+$ ) species is low and suddenly cooperative effects, when the density of  $\text{Fc}^+$  increases. For the comprehensive characterization of the structural properties, a combination of 3D electron diffraction (ED),<sup>[40,41]</sup> modeling, powder X-ray diffraction (PXRD) supported by density functional theory (DFT) calculations, was used to enable the structure determination of the fine-crystalline powder materials. Subsequently, electronic, optical, and redox properties were characterized using X-ray photoelectron spectroscopy (XPS) and PES on air (PESA), UV–vis, and photoluminescence.

## 2. Results and Discussion

### 2.1. Synthesis of Ferrovskites and Crystal Structure Determination by 3D Electron Diffraction

A systematic series of Fc-ligands capable of forming hybrid phases with lead halides was prepared first (**Figure 1a**, inset). The interaction of the Fc derivatives is achieved by an ammonium group. This head group can be attached to Fc-COOH by ester coupling chemistry as described in detail in the Experimental Section. Compared to the work of Zhang et al.,<sup>[35]</sup> our main intention for this particular molecular design is that the distance between the lead halide phase and Fc can be controlled by the adjustment of the length of the alkyl linker  $(\text{CH}_2)_n$  ( $n = 2,4,6$ ). However, such an ester group is capable of secondary intermolecular interactions such as hydrogen bonding. The oxygen-containing ester group provides a certain polarity to the molecule and can provide interactions to the ammonium head group.<sup>[42]</sup> The characterization of the molecular compounds was performed by standard techniques (see Figures S1–S4, Supporting Information). The described ligands are dissolved in dimethyl formamide (DMF) as a solvent together with a certain amount of lead bromide ( $\text{PbBr}_2$ ), forming a precursor solution. The formation of the novel hybrid phases, is initiated by an antisolvent method using dichloromethane (DCM) or toluene. The formation of a solid phase denoted as  $[\text{Fc}_n\text{Br}]^{\text{Pb}}$  can be observed when the precursor solution is added to the antisolvent. We designate the resulting phases as ferrovskites, as a reference to a ferrocene-containing perovskite.

The investigation of the precipitates by scanning electron microscopy (SEM) illustrates that small crystals form for all Fc-ligands (**Figure 1b–d**). The significant difference between the lateral extension of those crystals (several  $\mu\text{m}$ ) compared to

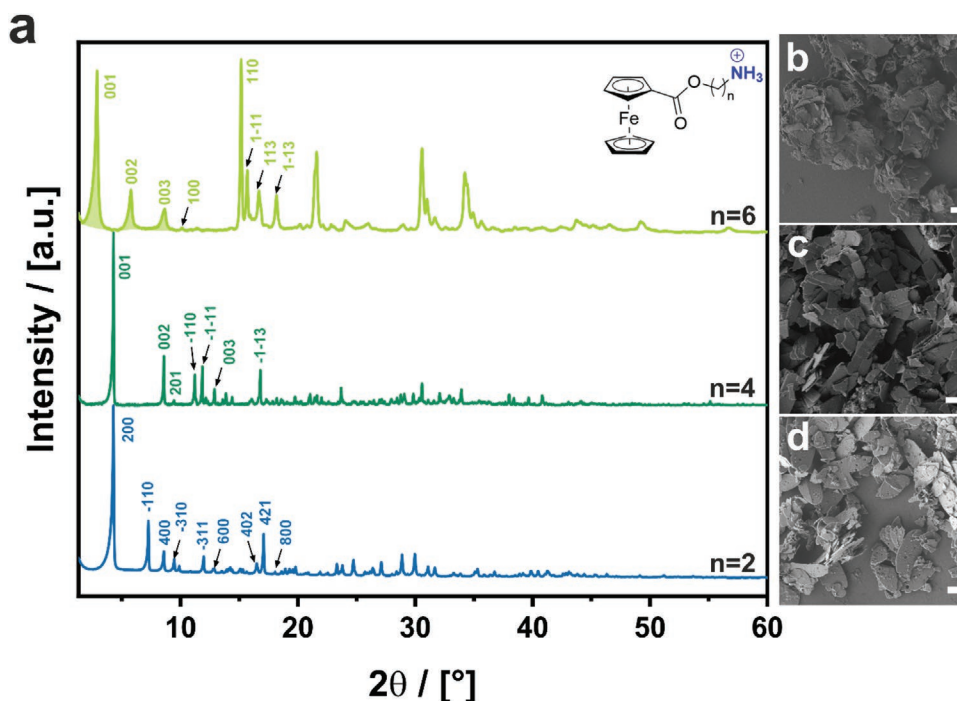


**Figure 1.** a) Experimental powder X-ray diffraction (PXRD) patterns for the reaction product of  $FcC_nBr$  and  $PbBr_2$  with chemical structure of the used Fc-derivatives with alkyl linkers of the length  $(CH_2)_n$  ( $n = 2, 4, 6$ ) as inset. Reflections were indicated based on crystal structure analysis, which will be discussed later. First three reflections (shaded in green) of  $n = 6$  have a FWHM values of  $\approx 0.26^\circ$ ,  $0.30^\circ$ , and  $0.40^\circ$   $2\theta$ . Scanning electron microscopy (SEM) images of the crystals formed with  $PbBr_2$  and b)  $FcC_6Br$ , c)  $FcC_4Br$ , and d)  $FcC_2Br$ . Scale bar = 2  $\mu m$ .

their thickness (nm range) is a first indication for the formation of layered structures. The lamellar nature of all three phases  $[FcC_nBr]^{Pb}$  ( $n = 2, 4, 6$ ) can in principal be confirmed by PXRD as shown in Figure 1a by the first strong reflections ((001) and (200), respectively), that can be assigned to the basal distances. However, the PXRD patterns are too complex to achieve an unambiguous characterization of the crystal structures. The crystals (Figure 1b–d) obtained in the antisolvent process are also too thin to perform classical single-crystal X-ray diffraction (SCXRD).

With such hybrid materials, it is essential to know the short and especially the long-range order to understand the interplay of structure and function. With the recent developed method 3D ED it is now possible to overcome the limitation of small crystal sizes and to solve structures of even nanocrystals.<sup>[43–45]</sup> In several cases, it could be demonstrated that beyond the structure solution, the consideration of dynamical scattering effects allows a precise structure refinement and the detection of hydrogen atoms.<sup>[46,47]</sup> In favorable cases it even approaches the accuracy of SCXRD and furthermore enables a robust determination of the absolute structure.<sup>[48,49]</sup> One challenge that still needs to be overcome is the beam sensitivity of some materials, which can make a structure analysis difficult or impossible. It could be shown that the development of fast acquisition protocols<sup>[45,50]</sup> allows the use of this technique with various transmission electron microscopes (TEMs) even for very beam sensitive materials.<sup>[41,51]</sup> Nevertheless, especially in hybrid layered systems, besides beam sensitivity, stacking disorder is another difficulty that often requires a combination of several methods such as 3D ED, PXRD, modeling/simulation, and DFT calculations.<sup>[41,52]</sup>

The solid phases of  $[FcC_2Br]^{Pb}$  and  $[FcC_4Br]^{Pb}$  have been investigated with 3D ED, resulting in the composition  $(FcC_2)PbBr_3$  and  $(FcC_4)_4Pb_3Br_{10}$ , respectively. The crystallographic details of all three phases are summarized in **Figure 2** and **Table 1** and will be discussed here in detail.

In case of  $(FcC_2)PbBr_3$  the structure analysis was attempted purely based on 3D ED data. Three crystals (Figure S5a–c, Supporting Information) have been measured with a very low accumulated electron dose<sup>[53,54]</sup> of  $\approx 2.5 e^- A^{-2}$  for each data set. The structure can be described in the monoclinic space group  $C 2/c$  with the lattice constants given in Table S1 (Supporting Information). To reduce dynamical scattering effects and to improve therewith the reflection statistics, three data sets were merged to be one ( $R_{int} = 10.6\%$ ). The structure could be solved ab initio based on each single dataset and enabled a clear identification of all non-hydrogen atoms (see Figure S7a–c, Supporting Information). The following kinematical refinement converged to a fairly low  $R_1(obs)$  value of 14.9%. As can be seen from the successful Rietveld refinement, the structure completely describes the crystalline parts of the sample (Figure S10a, Supporting Information). The overall crystallinity (Figure S8a, Supporting Information) and the resolution of the diffraction data was high enough to perform a dynamical refinement of the structure model resulting in an excellent overall  $R_1$  value of 9.4% for all observed reflections with highly improved geometry of the structure model compared to the kinematical refinement. This made it even possible to detect most of the hydrogen positions by the difference Fourier synthesis above the  $3\sigma$ -level of the electrostatic difference potential map  $[\Delta V(\mathbf{r})]$  as shown in Figure S9 (Supporting Information).

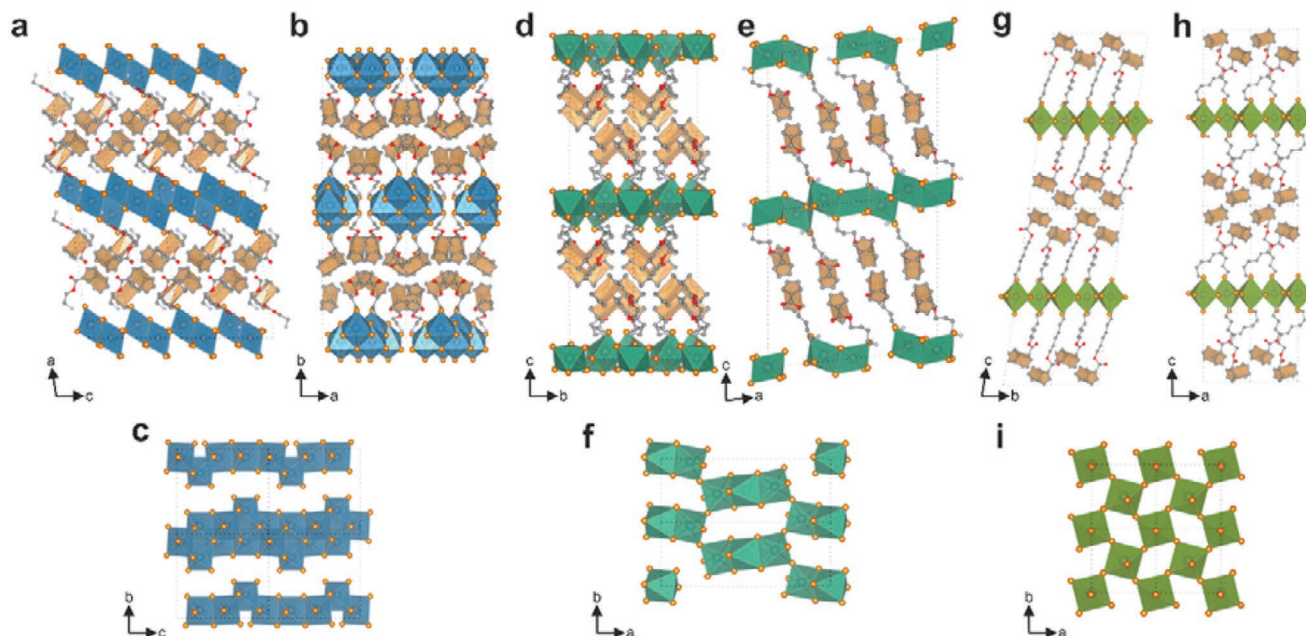


**Figure 2.** Crystal structures of a–c)  $(\text{FcC}_2)\text{PbBr}_3$  with edge-sharing octahedra in blue, d–f)  $(\text{FcC}_4)_4\text{Pb}_3\text{Br}_{10}$  with face- and corner-sharing octahedra in dark green, and g–i)  $(\text{FcC}_6)_2\text{PbBr}_4$  corner-sharing octahedra in light green. a, b, d, e, g, h) Side-view of the phases, c, f, i) top-view of the octahedra without Fc-ligands. Orange polyhedral represents the Fc-moieties. Hydrogen atoms have been removed for clarity.

The unit cell and symmetry of  $(\text{FcC}_4)_4\text{Pb}_3\text{Br}_{10}$  could as well be determined based on 3D ED and matches the PXRD data (see Figure 1a,  $n = 4$ ). The structure crystallizes in the monoclinic space group  $P 2_1/a$ . Five data sets needed to be merged to solve the structure ab initio. Besides the unambiguous determination

of the lead bromide network, the ferrocene positions could also be indicated (see Figure S7d–f, Supporting Information). For a following kinematical refinement, only the first 50 diffraction patterns of each of the three data sets were considered to exclude the diffraction patterns in which denaturation

**Table 1.** Crystal data for hybrid lead bromide phases with  $\text{FcC}_n\text{Br}$  ( $n = 2, 4, 6$ ), determined with 3D ED for  $n = 2, 4$  and modeling for  $n = 6$ . Lattice constants given here are based on Rietveld refinement and Pawley fit, respectively.

	$(\text{FcC}_2)\text{PbBr}_3$	$(\text{FcC}_4)_4\text{Pb}_3\text{Br}_{10}$	$(\text{FcC}_6)_2\text{PbBr}_4$
Precursor salt			
Empirical formula	$(\text{C}_{13}\text{H}_{16}\text{FeNO}_2)\text{PbBr}_3$	$(\text{C}_{15}\text{H}_{20}\text{FeNO}_2)_4\text{Pb}_3\text{Br}_{10}$	$(\text{C}_{17}\text{H}_{24}\text{FeNO}_2)_2\text{PbBr}_4$
Formula weight [ $\text{g mol}^{-1}$ ]	721.03	2630.44	1187.88
Crystal system	Monoclinic	Monoclinic	Triclinic
Space group	$C 2/c$	$P 2_1/a$	$P \bar{1}$
Z	16	2	2
$a$ [Å]	41.6677 (13)	22.3384 (10)	8.287 (5)
$b$ [Å]	12.7153 (4)	8.43444 (19)	8.284 (4)
$c$ [Å]	14.0140 (4)	20.6965 (7)	31.09 (3)
$V$ [Å <sup>3</sup> ]	7333.9 (4)	3877.3 (2)	2113 (3)
$\alpha, \beta, \gamma$ [°]	90, 98.9741 (11), 90	90, 96.109 (3), 90	81.97 (16), 90.62 (9), 89.83 (5)
$\rho$ [ $\text{g cm}^{-3}$ ]	2.61	2.25	1.86
$d_{\text{Fe-Fe}}$ [Å]	6.35 (5) <sup>a)</sup>	6.24 (5) <sup>a)</sup>	6.14 (4)
$E_{\text{gap}}$ [eV]	3.51 <sup>b)</sup>	3.27 <sup>b)</sup>	3.06 <sup>b)</sup>

<sup>a)</sup>For the structure determination at 97 K; <sup>b)</sup>Energy of the bandgap was determined by reflectance spectroscopy with a Kubelka-Munk plot provided in the Figure S13 (Supporting Information).



by the electron beam was already advanced. The refinement converged to  $R_1(\text{obs}) = 18.3\%$ . Details can be found in the section *3D electron diffraction data reconstruction and Structure refinement of  $(\text{FcC}_4)_4\text{Pb}_3\text{Br}_{10}$*  in the Supporting Information. The same data were used to perform a dynamical refinement resulting in an overall  $R_1$  value of  $11.7\%$  for all observed reflections. Even though the error values of structure refinement based on electron diffraction appear subordinate, the low completeness (Figure S6d–f, Supporting Information) and overall data quality is too low (see Figure S8b, Supporting Information) to verify the structure just based on 3D ED alone. Therefore, the structure has also been confirmed by a subsequent Rietveld refinement (Figure S10b, Supporting Information).  $15.2\%$   $\text{PbBr}_2$  was detected as an impurity in the sample.

In contrast to the phases  $(\text{FcC}_2)\text{PbBr}_3$  and  $(\text{FcC}_4)_4\text{Pb}_3\text{Br}_{10}$ , the beam sensitivity of  $[\text{FcC}_6\text{Br}]^{\text{Pb}}$  is so much increased, that it was not possible to collect a single ED pattern before degeneration of the crystal structure. In addition, the strongly pronounced plate-like morphology as shown in the SEM image (Figure 1b) gives reason to assume weakened interactions between the layers. From the broadened reflections indicated by the large full width at half-maximum (FWHM) of the first three reflections ( $\text{FWHM} > 0.25^\circ 2\theta$ ) of the PXRD pattern (see Figure 1a,  $n = 6$ ), it can already be assumed that the amount of stacking faults is significantly increased at this chain length ( $\text{FcC}_6$ ). However, from the intensity distribution of the profile in the  $2\theta$  range between  $12^\circ$  and  $40^\circ$  of the PXRD pattern (Figure S11, Supporting Information,  $n = 6$ ), it can be deduced that  $[\text{FcC}_6\text{Br}]^{\text{Pb}}$  is a Ruddlesden–Popper phase with the composition  $(\text{FcC}_6)_2\text{PbBr}_4$ .<sup>[34]</sup> A structure was modeled and optimized by DFT-D (see Figure 2, Table 1; Figure S12, Supporting Information).

Based on the crystal structure analysis, it can be confirmed that all phases are layered structures. To understand the electronic and optical properties of the materials, their crystalline structure is described in more detail below. In the structure of  $(\text{FcC}_2)\text{PbBr}_3$ , lead bromide octahedra are connected via their edges, forming a ribbon-like structure (Figure 2a–c). Four octahedra are connected to form a tetramer. A staggered arrangement of the tetramers leads to a zig-zag like structure of the  $[\text{PbBr}_3]^-$ -ribbons, which extend along the  $c$ -axis. The structure complies with the  $(\text{NH}_4)\text{CdCl}_3$  structure type,<sup>[55]</sup> but it has not been observed before for any hybrid lead halide material. This unusual arrangement of the octahedra is a consequence of the intermolecular interaction between the ferrocene groups and their resulting arrangement. Adjacent ferrocenes are positioned perpendicular to each other which is very similar to the arrangement in the crystal structure of non-substituted Fc.<sup>[56]</sup> In addition, it can be observed that one of the ammonium head groups located above a  $[\text{PbBr}_3]^-$ -ribbon are connected to the ester group of an adjacent ligand by hydrogen bonding (N1–H–O3) (see Figure S9, Supporting Information). The other ammonium head group (N2), on the other hand, adheres deeper in the  $[\text{PbBr}_3]^-$ -ribbon and does not form an N–H–O hydrogen bond. Thus, there is an intramolecular competition for the interaction of the ammonium group with the lead bromide framework. Therefore, it can be concluded that  $\text{FcC}_2\text{Br}$  acts as a strong structure-directing agent for the way the lead bromide octahedra are connected. The conformational flex-

ibility is increasing for longer alkyl linkers of  $\text{FcC}_n\text{Br}$ , and this will stepwise reduce the structure-directing character of the Fc constituent.

The reduced constraints in the packing of the ferrocene moieties allow the formation of a 2D structure in the lead bromide subphase in  $(\text{FcC}_4)_4\text{Pb}_3\text{Br}_{10}$  (Figure 2d–f). The inorganic layers contain trimers of face-sharing octahedra  $[\text{Pb}_3\text{Br}_{10}]^{4-}$  linked through bridging bromides to adjacent trimers. The inorganic sublattice resembling the  $\text{Cs}_4\text{Mg}_3\text{F}_{10}$  structure<sup>[57]</sup> was reported before for other hybrid lead halides such as compounds containing phenyltrimethylammonium bromide  $(\text{C}_6\text{H}_5\text{N}(\text{CH}_3)_3\text{Br})$ <sup>[58]</sup> or trimethylsulfonium bromide  $(\text{CH}_3)_3\text{SBr}$ .<sup>[59]</sup> This results in a periodic layered structure in which the inorganic and organic phases are arranged alternately, similar to Ruddlesden–Popper phases.<sup>[59]</sup>

If the alkyl linker becomes even longer, as in  $(\text{FcC}_6)_2\text{PbBr}_4$ , a Ruddlesden–Popper phase<sup>[60]</sup> is formed. The reflection positions of the simulated PXRD diagram (Figure S12, Supporting Information) of the modeled structure largely match those of the experimental PXRD diagram, but the intensity ratios differ significantly in some cases, so that a crystal structure description is only possible to an approximate extent. The formation of a hydrogen bond to the ester function is likely to be suppressed with longer alkyl chain of the linker, so that the ammonium is now completely available for interaction with the inorganic phase. It is also likely that the neighboring ferrocene groups can pack more efficiently, forming a layer of their own, alongside the organic linker- and inorganic  $[\text{PbBr}_4]^{2-}$  layer, in a less densely packed crystal structure (Figure 2g–i).

## 2.2. Electronic and Optical Properties of Ferrovskites

Because it is known from the literature that the bandgap strongly depends on the type of linkage of the  $[\text{PbBr}_6]^{4-}$  octahedra,<sup>[19,29]</sup> following a trend of “corner-sharing < edge-sharing < face-sharing”, we also expect such an effect for the ferrovskite phases described in the previous section. Optical reflectance spectroscopy (ORS) was used to determine the bandgap of the resulting materials (Figure 3a; Figure S13, Supporting Information).

For  $(\text{FcC}_2)\text{PbBr}_3$ , which is composed of edge-sharing octahedra seen in Figure 3c, the largest bandgap is found with  $3.51\text{ eV}$  ( $\Rightarrow \lambda = 353\text{ nm}$ ). For the phase  $(\text{FcC}_4)_4\text{Pb}_3\text{Br}_{10}$ , a bandgap at  $3.27\text{ eV}$  ( $\Rightarrow \lambda = 379\text{ nm}$ ) is found, which is in good agreement with the literature.<sup>[59]</sup> Interestingly, the phase with a mixture of face- and corner-sharing octahedra (Figure 3d) has a smaller bandgap than the edge-sharing  $(\text{FcC}_2)\text{PbBr}_3$ . As expected, the obtained Ruddlesden–Popper phase  $(\text{FcC}_6)_2\text{PbBr}_4$ , containing only corner-sharing octahedra (Figure 3e) shows the smallest bandgap with  $3.06\text{ eV}$  ( $\Rightarrow \lambda = 405\text{ nm}$ ). These values are in good agreement with the literature.<sup>[61]</sup> The relative energies of the valence band maximum (VBM) and conduction band minimum (CBM) were obtained from photoelectron spectroscopy in air (PESA) measurements (Figure S14, Supporting Information). The combined results are given in Figure 3a. The VBM is almost constant for all lead bromide phases with a slight trend toward lower energies from  $(\text{FcC}_2)\text{PbBr}_3$  to  $(\text{FcC}_6)_2\text{PbBr}_4$ . Thus, it can be seen that the change of  $E_{\text{gap}}$  is mainly an effect of the

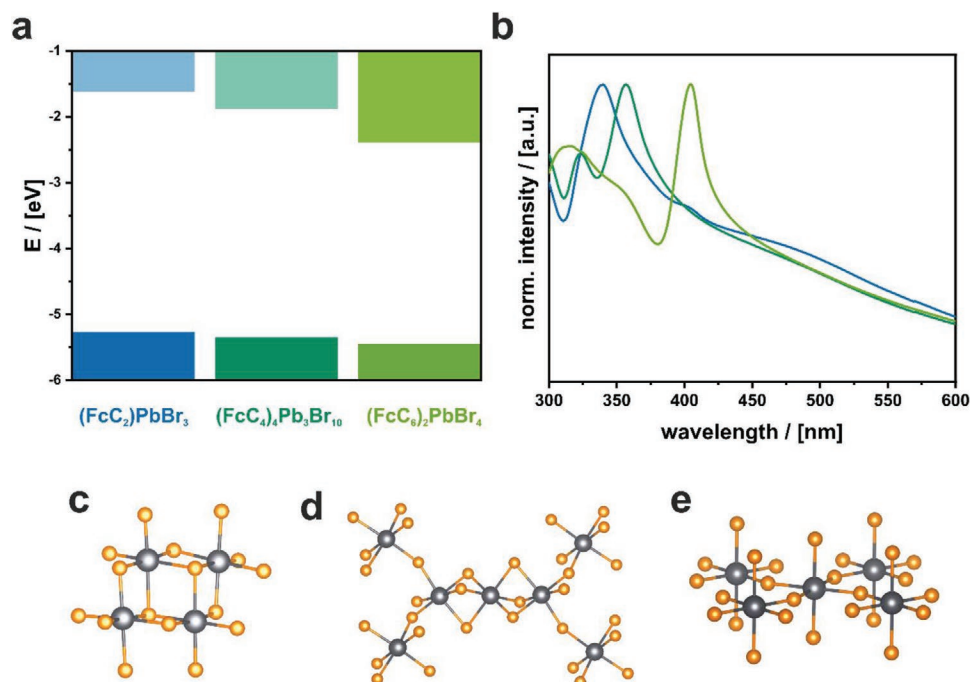


**Figure 3.** a) Band structure analysis determined from ORS/Kubelka-Munk and PESA measurements on the different ferrovskite materials. b) Absorption spectra of the particles dispersed in toluene. Arrangement of lead halide octahedra in the different ferrovskite phases: c)  $(\text{FcC}_2)\text{PbBr}_3$  with edge-sharing octahedra, d)  $(\text{FcC}_4)_4\text{Pb}_3\text{Br}_{10}$  with face- and corner-sharing octahedra, and e)  $(\text{FcC}_6)_2\text{PbBr}_4$  with only corner-sharing octahedra.

structure of the lead halide phase on the CBM, which decreases significantly in the given series (Figure 3a).

UV-vis absorption spectra can be recorded from a dispersion of the particles in toluene (Figure 3b). The advantage of toluene as a solvent is that its absorption bands are ( $\lambda_{\text{abs}} < 280$  nm) are in a different region than  $E_{\text{gap}}$ , respectively,  $\lambda_{\text{abs}}(\text{FcC}_n\text{Br})$ ; see Figure S4 (Supporting Information). Furthermore, the ferrocene ligands  $\text{FcC}_n\text{Br}$  are insoluble, and it can be assumed that they will remain in the ferrovskite crystals. Ferrocene has a very low extinction coefficient, which is why the absorption of the ligands is barely detected.<sup>[62]</sup> Between 450 and 500 nm a slight shoulder of the Fc-ligands is found, which represents the HOMO  $\rightarrow$  LUMO transition. Significantly stronger absorption is observed for the near-band-edge states with strong resonance peaks in all compounds. The absorption maximum but also the width of the absorption peaks provide information about the excitons and their binding energy. The peaks of the excitonic resonance are clearly separated from the continuous absorption, suggesting strongly bound excitons. Excitonic bandgaps for  $(\text{FcC}_2)\text{PbBr}_3$  showing a maximum at 337 nm, for  $(\text{FcC}_4)_4\text{Pb}_3\text{Br}_{10}$  with a maximum at 357 nm and  $(\text{FcC}_6)_2\text{PbBr}_4$  with a maximum at 405 nm are found. Interestingly,  $(\text{FcC}_4)_4\text{Pb}_3\text{Br}_{10}$  shows a blueshifted maximum at 323 nm which is attributed to material defects in the structure.<sup>[59]</sup>

It is noticeable that the peaks become narrower and sharper with a longer head group of the Fc-ligand. Mainly two effects define the excitonic binding energy in low-dimensional organic-inorganic materials: the quantum confinement and the dielectric confinement. From the ribbons of  $(\text{FcC}_2)\text{PbBr}_3$ , over the perovskite-like  $(\text{FcC}_4)_4\text{Pb}_3\text{Br}_{10}$  to the Ruddlesden-Popper type  $(\text{FcC}_6)_2\text{PbBr}_4$ , the quantum confinement of the generated

excitons shrinks. On the other hand, the Fc-ligands define the dielectric environment and influence the screening of the Coulombic attraction between the exciton's hole and electron. The length of the head group plays a crucial role for the proximity to the inorganic phase and thus also the influence of the dielectric constant of the organometallic molecules. The closer the Fc-ligands are to the inorganic phase, the stronger the confinement.

Up to this point, it seems that the ferrocene moiety is more or less inactive regarding the electronic properties of the phases. Is it just an overdone linker? A first indication that the ferrocene is more, comes from the PL spectra. Hybrid lead halide phases show intense PL because of their direct bandgap character. The quantum confinement enables the formation of self-trapped excited states which show a strong Stokes-shift and broadband (white light) emission.<sup>[63,64]</sup> However, we could not detect any PL signals for  $(\text{FcC}_2)\text{PbBr}_3$  and  $(\text{FcC}_4)_4\text{Pb}_3\text{Br}_{10}$ ; see, for instance, Figure 5d for  $(\text{FcC}_2)\text{PbBr}_3$ . In agreement with studies on functional materials containing ferrocene in the literature,<sup>[65]</sup> the explanation for the effect is photoluminescence quenching by efficient photoinduced electron transfer (PET) to the ferrocene. The efficiency of PET depends on the distance between donor and acceptor. This distance is largest in the case of  $(\text{FcC}_6)_2\text{PbBr}_4$ , and actually a weak emission can be observed at  $\lambda = 416$  nm ( $E_{\text{PL}} = 2.98$  eV; data are shown in Figure S15, Supporting Information).

Because of the PET process, our hypothesis is that the optoelectronic properties of ferrovskites will change, if we change the electronic properties of the Fc entity. Because the vicinity between inorganic and metal-organic phase is closest for the new  $(\text{FcC}_2)\text{PbBr}_3$  structure, we will concentrate our work on this compound from here on.

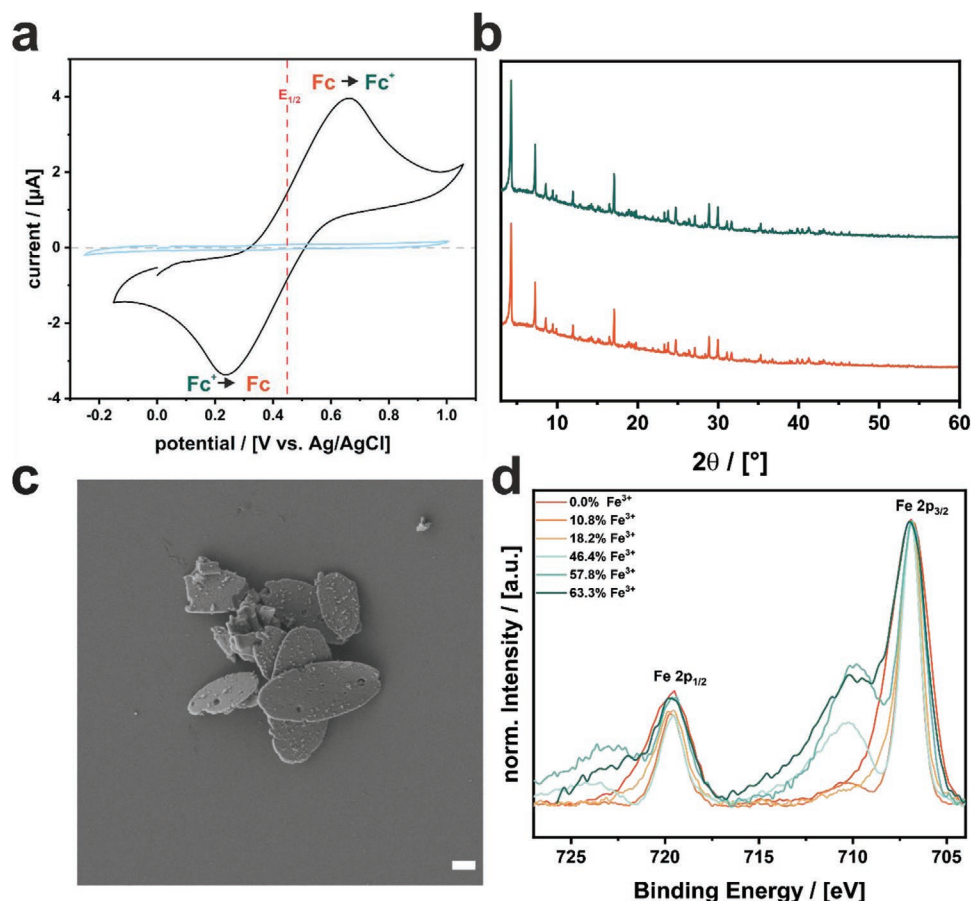


**Figure 4.** a) Cyclic voltammogram (CV) of  $(\text{Fc}_2)\text{PbBr}_3$  (black) on ITO (light blue) at scan speed of  $10 \text{ mV s}^{-1}$  in  $0.1 \text{ M LiTFSI}$  in  $\text{HFE}:\text{DEC} = (97:3)$ , a halfwave potential at  $E_{1/2} = 0.45 \text{ V}$  is found. For a detailed description of the measurement, we refer to the Experimental Section. b) PXRD measurement of the particles before oxidation (bottom) and after oxidation (top) with  $57.8\% \text{ Fe}^{3+}$ . c) SEM image of the particles after oxidation with  $57.8\% \text{ Fe}^{3+}$ . d) Normed X-ray photon spectroscopy (XPS) measurements for Fe  $2p_{1/2}$  and Fe  $2p_{3/2}$  of oxidized particles with increasing  $\text{Fe}^{3+}$  content. For the quantitative evaluation of the signals we refer to Figure S19 (Supporting Information). The color coding of the varying  $\text{Fe}^{3+}$  contents is used for further diagrams and is no longer specified there.

### 2.3. Defect Creation by Redox-Chemistry and Electro spectroscopic Consequences

An effective way to change the electronic property of the Fc building block is oxidation to ferrocenium ( $\text{Fc}^+$ ). If only few ferrocenium molecules are oxidized, assuming there is an electronic communication between the subphases, a point defect will be created which may induce doping or other electronic effects (see Scheme 1). Furthermore, it will be interesting to successively increase the fraction of  $\text{Fc}^+$ . We hope that cooperative effects can occur at a critical density of  $\text{Fc}^+$  and due to the periodic arrangement of the ligands.

Cyclic voltammograms (CV) are recorded to study the oxidation of Fc-containing materials, as they provide information about the redox process of the Fc-ligands and the electronic processes in the material. A suitable electrolyte for the electrochemical characterization of hybrid perovskites is a mixture hydrofluoroether (HFE) and diethyl carbonate (DEC) with lithium bistrifluoromethane sulfonimide ( $\text{LiTFSI}$ ), proposed by Hasan et al.<sup>[66]</sup> The lithium containing electrolyte is commonly used for lithium ion batteries and does not dissolve  $(\text{Fc}_2)\text{PbBr}_3$ .

In the initial material the ligand is present in pure, nonoxidized form according to Mössbauer spectroscopy (Figure S16 and Table S3, Supporting Information). Figure 4a shows the recorded CV of  $(\text{Fc}_2)\text{PbBr}_3$  drop-casted on ITO (in  $0.1 \text{ M LiTFSI}$  in  $\text{HFE}:\text{DEC} = (97:3)$ , scan speed  $10 \text{ mV s}^{-1}$  after purging with  $\text{N}_2$  to remove dissolved oxygen). ITO was measured as a reference, which shows that the substrate is electrochemically inactive under chosen conditions (Figure 4a, light blue). The CV measured for  $(\text{Fc}_2)\text{PbBr}_3$  fits well to reports in the literature about other functional materials containing ferrocene.<sup>[37,67]</sup> Redox peaks centered at  $E_{1/2} = 0.45 \text{ V}$  are found, indicating that the Fc-ligands are electrochemically addressable. The signal of the oxidation at  $0.65 \text{ V}$  as well as the signal of the reduction at  $0.24 \text{ V}$  shows no asymmetries, which indicates an ordinary electron transfer between the electrolyte and Fc-ligand.<sup>[68]</sup> Because there are no additional signals, we assume that the inorganic  $[\text{PbBr}_3]^-$  constituent is electrochemically inactive in the relevant voltage range.

While the electrochemical methodology (CV) is suitable to clarify the redox activity of Fc in the ferrovskites, only a very small amount of sample is affected and the ratio of oxidation

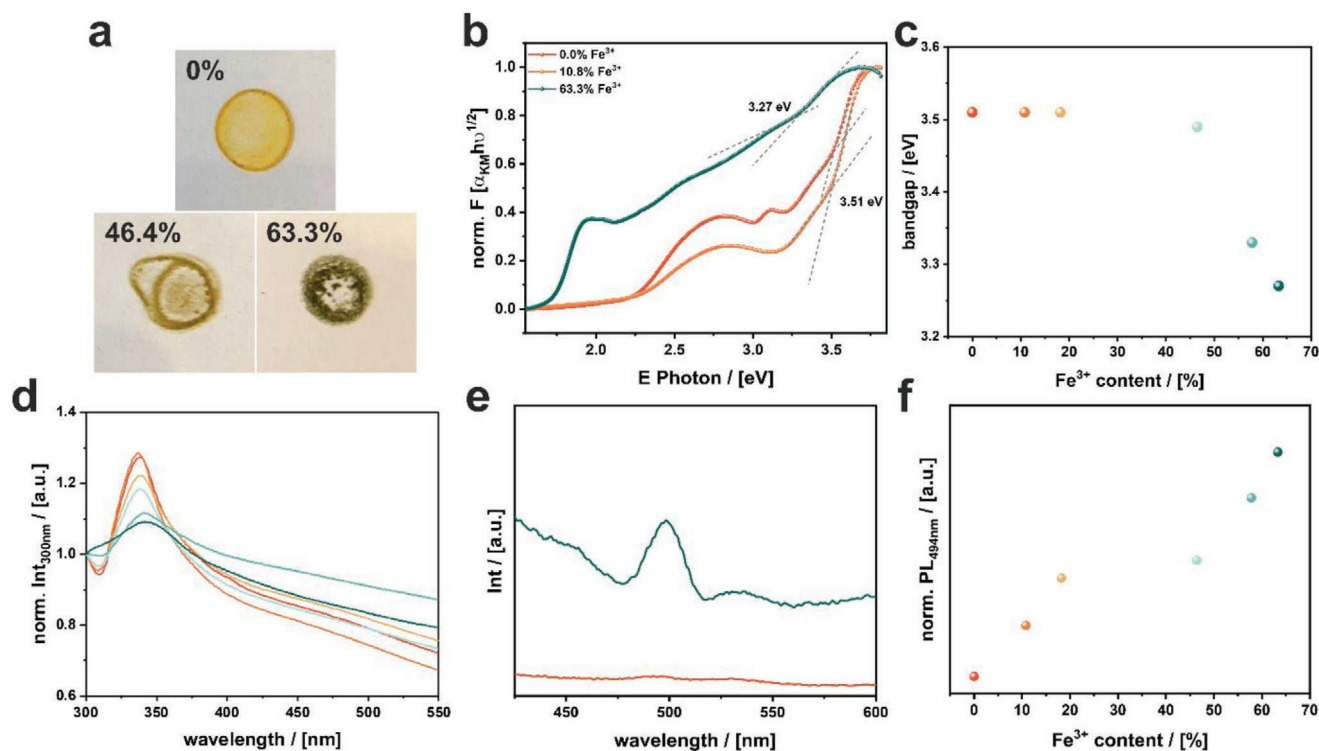


**Figure 5.** a) Photograph of drop-casted particles with varying  $\text{Fe}^{3+}$  content. b) Normalized Kubelka-Munk (KM) plot of  $(\text{Fc}_2)\text{PbBr}_3$  before and after oxidation. Other KM plots are shown in Figure S21 (Supporting Information). c) Bandgap determined from KM of  $(\text{Fc}_2)\text{PbBr}_3$  with increasing  $\text{Fe}^{3+}$  content. d) Optical absorption of particles dispersed in toluene. e) Photoluminescence signal before (orange) and after (green) oxidation of the particles with excitation at 310 nm and f) photoluminescence of normed PL intensity at 494 nm with varying  $\text{Fe}^{3+}$  content.

to  $\text{Fc}^+$  is hard to control because of an ill-defined contact of the  $(\text{Fc}_2)\text{PbBr}_3$  particles with the electrode. Therefore, the chemical oxidation of dispersed  $(\text{Fc}_2)\text{PbBr}_3$  particles in a solvent using perchlorate ( $\text{ClO}_4^-$ ) was attempted. A detailed description of the oxidation is given in the Experimental Section and in the Supporting Information (Figures S17+S18, Supporting Information). The investigation of the samples before and after oxidation by PXRD (Figure 4b) and SEM (Figure 4c; compare to Figure 1d) shows no changes indicating that the ferrovskite is stable. Whether oxidation has occurred and whether the  $\text{Fc}^+/\text{Fc}$  ratio can be controlled by the amount of oxidant used were verified by XPS shown in Figure 4d. It is obvious that the signals for  $\text{Fe}^{3+}$ , e.g.,  $E(\text{Fe-}2p_{3/2}) = 710.25 \text{ eV}$  become more and more intense. The quantification of the XPS spectra reveals that the  $\text{Fc}^+/\text{Fc}$  ratio ranges from 0 % to 63.3 %; see Figure S19 (Supporting Information). A higher oxidation degree is not possible because the samples seem to restructure if even more perchlorate is used.

## 2.4. Defect-Density/Optoelectronic Correlations in Ferrovskites

Ferrocenium has a different color than ferrocene. Due to the oxidation, an electron of the  $e_{2g}$  molecular orbital in Fc is removed. A ligand-to-metal charge-transfer transition occurs in  $\text{Fc}^+$ , resulting in an absorption band at 631 nm (1.97 eV) and a color change from orange to green/blue (see Figure S20a, Supporting Information).<sup>[69]</sup> Therefore, it is not surprising

that also the ferrovskite samples have a different color after oxidation (Figure 5a). Their appearance changes from orange to green. However, the important question is, if there is some sort of coupling of the electronic states of  $\text{Fc}^+$  with the inorganic subphase. Optoelectronic properties of  $(\text{Fc}_2)\text{PbBr}_3$  were examined with a combination of optical absorption/reflectance and photoluminescence spectroscopy. Our data show that it is necessary to distinguish between samples with a low content of  $\text{Fc}^+$  (Scheme 1b) and a high content (Scheme 1c).

If the  $\text{Fc}^+/\text{Fc}$  ratio is low, ferrocenium is a point defect randomly distributed in the  $(\text{Fc}_2)\text{PbBr}_3$  phase. The bandgap energy of the samples was obtained from ORS measurements of the dried powder samples (Figure 5b; Figure S21 Supporting Information). It can be seen that the bandgap remains constant at  $\approx 3.5 \text{ eV}$  (Figure 5c) up to  $\text{Fc}^+/\text{Fc} = 45 \%$ . Optical absorption spectra were recorded for a dispersion of the oxidized ferrovskite particles. The results are shown in Figure 5d. The increase of the absorption in the range  $\lambda > 425 \text{ nm}$  is caused by the presence of the oxidized species  $\text{Fc}^+$ . There are also some effects on the excitonic peak of the lead bromide subphase at 337 nm. The excitonic peak is broadened, which can be explained by the change of the dielectric environment.<sup>[59]</sup> Oxidation results in a change in polarization and the excitons become even more confined as the relative permittivity of the ligand alters. However, not only a color change is observed, after the oxidation  $(\text{Fc}_2)\text{PbBr}_3$  shows an emission at 494 nm with excitation at 310 nm, presented in Figure 5e. The intensity of the signal increases for an increasing oxidation degree (Figure 5f). The resulting



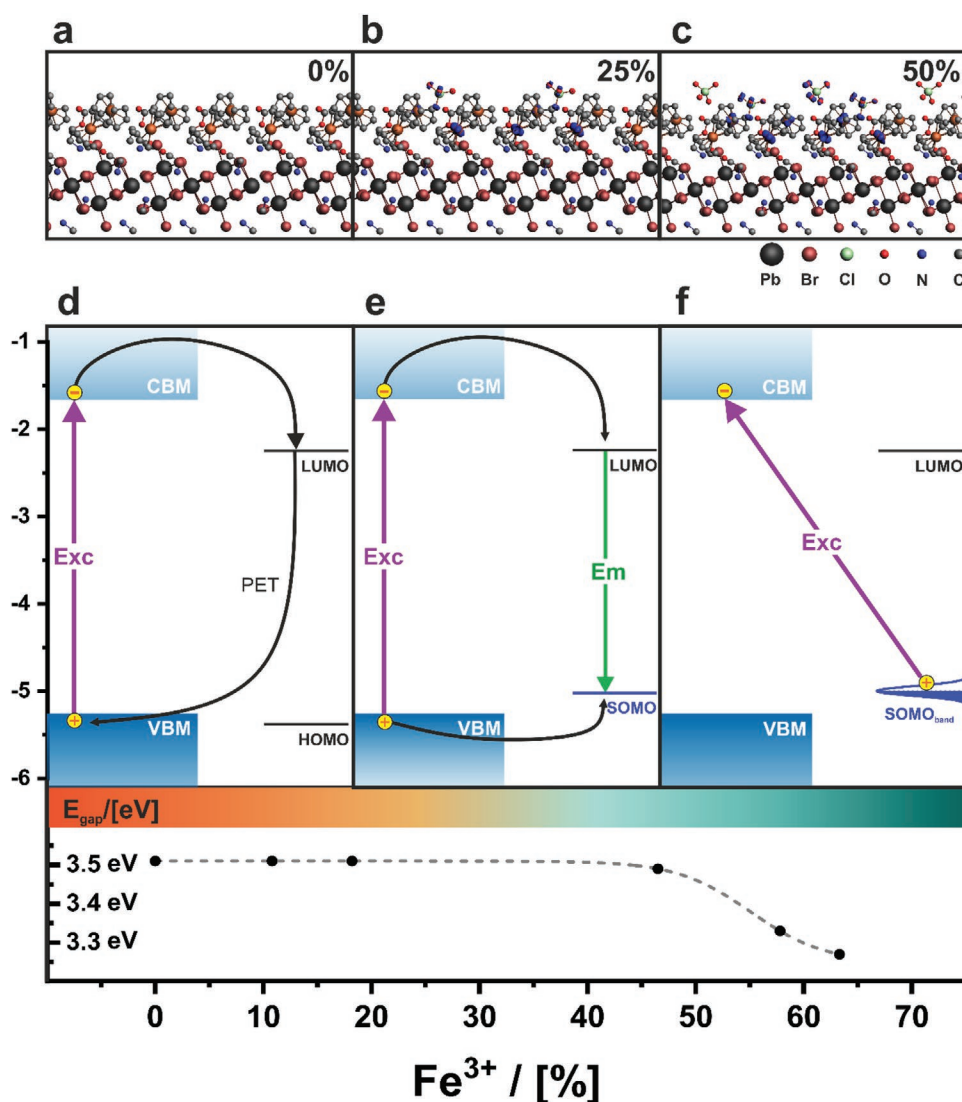


**Figure 6.** Representation of the ab initio calculations using the BAND code for a) the intrinsic  $(\text{Fc}_2)\text{PbBr}_3$ , b) with 25% of the ligands oxidized with  $(\text{ClO}_4)^-$ , c) with 50% of the ligands oxidized with  $(\text{ClO}_4)^-$ . The location of the unpaired paramagnetic spin was calculated and made visible in spin density (blue isosurface). Hydrogen atoms were removed for clarity; experimentally determined band structure of  $(\text{Fc}_2)\text{PbBr}_3$  d) in the intrinsic state showing why PET occurs upon excitation (Exc) at 310 nm, e) after the oxidation with  $(\text{ClO}_4)^-$  at low oxidation degrees [radiative recombination/emission (Em) occurs due to the new energy alignment of the single occupied molecular orbital (SOMO)] and f) at high oxidation degrees with the emergence of the new  $\text{SOMO}_{\text{band}}$ .

luminescence peak is attributed to the oxidized Fc-ligand, which shows emission at 514 nm in solution (Figure S20b, Supporting Information). We were also able to demonstrate this effect by electrochemical oxidation, shown in Figure S22+S23, Supporting Information. The excitation spectrum recorded for  $[\text{Fc}_2\text{Br}]^+$  as a reference shown in Figure S20b (Supporting Information) demonstrates that this fluorescence cannot be stimulated by excitation at 310 nm. Therefore, we assume that there is an electron transfer from the semiconductor to the  $\text{Fc}^+$ -ligand with subsequent radiative recombination. To support this assumption, we determined the relative energies of HOMO and LUMO of  $\text{Fc}_2\text{Br}$  before oxidation using a combination of UV-vis spectroscopy and PESA (see Figures S4a and S20c, Supporting Information). **Figure 6** shows the alignment of the bands and MOs before (d) and after oxidation at low  $\text{Fc}^+/\text{Fc}$

ratio (e). The step-like arrangement of energies before oxidation shows well why PET is observed. The LUMO of the Fc-ligand is below the CBM, which is why excited electrons move to the acceptor level. The recombination of charge carriers is non-radiative because the hole from the CBM cannot move to the HOMO. After oxidation, the situation changes. The oxidation only affects the position of the emerging single occupied molecular orbital (SOMO;  $e_{2g}$ ), which now has a higher energy than the previous HOMO ( $a_{1g}$ , which is now below  $e_{2g}$ ).<sup>[70]</sup> We assume that the position of the LUMO does not change and determine the position of the SOMO from the observed photoluminescence. Again, the excitation of the semiconductor at 310 nm transfers an electron from the CBM to the LUMO, but since the SOMO is now above the CBM, the generated hole can be transferred as well. As the MO arrangement changes, their

energies now lie favorably within the bandgap,<sup>[30]</sup> thus, radiative recombination is observed.

There is a critical value in Fe<sup>3+</sup> content, when the optical absorption of the material changes more severely. The KM plots for (FcC<sub>2</sub>)PbBr<sub>3</sub> with Fc<sup>+</sup>/Fc = 63.3 % derived from the optical measurements are shown in Figure 5b (green). There is a fundamental change compared to the native (FcC<sub>2</sub>)PbBr<sub>3</sub> and the weakly oxidized samples (Figure 5b, 10.8 % Fe<sup>3+</sup>). A new feature at 2.0 eV appears, which can be assigned to the large number of Fc<sup>+</sup> species. The bandgap, given by the inorganic lead-bromide network can be determined by the intersection of two linear regression lines. Interestingly, a flattening of the slope and a narrowing of the bandgap is observed above an Fe<sup>3+</sup> content of about 50% (Figure 5c). Bandgap narrowing is usually observed in heavily doped semiconductors, where discrete impurity levels in the bandgap of the semiconductor evolve an impurity band, which can overlap with the CB or VB.<sup>[12,71,72]</sup> Here it seems that the electronic situation of the semiconductor changes abruptly as soon as enough Fc-ligands have been oxidized. Essentially, our measurements show that the material with a high number of Fc<sup>+</sup> defects is an entirely different semiconductor. We assume, that this is related to electronic coupling between [PbBr<sub>3</sub>]<sup>-</sup>-ribbons and the ligand layer and within the ligand layer. Unfortunately, a detailed quantum chemical study of this coupling for this complex system via accurate band structure calculations is extremely difficult as this is already the case for less complex systems.<sup>[73]</sup>

It is nevertheless interesting to get some idea about the electron hopping from the ligand layer to the ribbon and at least within the ligand layer since this might be important for the understanding of the SOMO band discussed above (Figure 6f). Several quantum chemical calculations have been published in the literature concerning the electron transfer from surfaces into ligands with ferrocene moieties from C60,<sup>[74]</sup> diamond,<sup>[75]</sup> or semiconductor colloids.<sup>[76]</sup> Tarafder et al. have studied hole transfer from a photoexcited CdSe nanorod to a single Fc-ligand tethered to its surface. They discussed the results by quantum chemical calculations based on DFT using GW corrections within a Marcus charge transfer model.<sup>[77]</sup> However, less is known about quantum chemical based charge transfer calculations within a layer of ligands as in our systems.

To investigate charge localization and electron transfer possibilities between Fc (Fe<sup>2+</sup> centers) and Fc<sup>+</sup> (Fe<sup>3+</sup> centers), we have set up a simplified theoretical model structure shown in Figure 6a–c. In a first step, we have thereby extracted a layer from the experimentally determined unit cell consisting of [PbBr<sub>3</sub>]<sup>-</sup>-ribbons and surrounding Fc-ligands. The structure with eight [PbBr<sub>3</sub>]<sup>-</sup> units is surrounded by four FcC<sub>2</sub>-ligands on one side of the ribbon and four methylammonium ligands on the other side as shown in Figure 6a.

This structure can serve as a surface model containing only Fe<sup>2+</sup> sites. To change some of the Fe<sup>2+</sup> sites into Fe<sup>3+</sup> sites one has to obey the electrochemical charge neutrality principle.<sup>[78]</sup> As the cationic charges are balanced in the experiment by perchlorate, we have added perchlorate units to the surface of our theoretical model structure, as illustrated in Figure 6b,c.

In a simple physicochemical picture, the perchlorate forms an adsorbed anion layer in an outer Helmholtz plane, while the nearest Fe<sup>3+</sup> center in the ligand layer might be supposed at the

first place to balance the negative charge. In this way one might provide a rough model for the material surface in the experiments, however, the localization of charge in the ligand layer turns out to be more complex when quantum chemical calculations within the SCM modeling suite using the BAND code on Perdew–Burke–Ernzerhof (PBE) and nonrelativistic double zeta theory level were performed.<sup>[73,79,80]</sup>

First geometry optimization provided the final structures shown in Figure 6a–c and then information about the charge distribution was extracted using a Hirshfeld charge analysis.<sup>[81–83]</sup> Although absolute Hirshfeld charge values can deviate for some atoms from the formal charges one would expect from the oxidation states, one can use them to track changes in charge distributions when perchlorate units are added. The Hirshfeld charges are therefore used for a qualitative discussion of the change in charge distribution when the Fe<sup>3+</sup>/Fe<sup>2+</sup> ratio is increased by the addition of perchlorate.

Through this ground state analysis (see Figure S24, Supporting Information) with a single perchlorate anion (Figure 6b) one finds enhanced positive Hirshfeld charges at the Fe center which lies closest to the perchlorate and to a lesser degree on the neighboring Fe sites. Not surprisingly the positive charge is not fully localized at a single Fe site.

This can also be shown by ground state spin density calculation, shown in Figure 6b. The spin density is not localized at a single Fe site, as would be expected for a single Fe<sup>3+</sup> with spin ½. It is partially distributed over the neighboring sites. This means that a surface adsorbed perchlorate anion is not able to localize a full positive counter charge, i.e., at a single Fe<sup>3+</sup> site.

For a further discussion of this problem, one can consider the limiting case where a perchlorate anion would be able to localize a positive charge  $q = e$  fully at its closest Fe-site and hence generates a Fe<sup>3+</sup> center (Fc<sup>+</sup>). As the DFT results show that this is not the electronic ground state, one is forced to think in terms of electron hopping from neighboring Fe<sup>2+</sup> sites (Fc) aiming to neutralize the positive charge. This would lead to a decrease in the positive charge  $q < e$  at the center and increase of charge at the neighboring sites and provide a ground state with a partially delocalized charge over the neighboring sites.

Even in our simple model in Figure 6b, one would have to consider four sites and at least three electrons to be distributed. One might also think in terms of a single hole at four sites. Then the hole would be mainly localized at the site closest to the perchlorate anion.

In reality, much more sites and much more electrons (or holes) would have to be considered. However despite this problem, one can at least try to provide a rough estimate of single electron (or hole) transfer rates using a Marcus model.<sup>[77]</sup> In this model, the charge is initially confined in a Marcus model fragment (i.e., Fc<sup>+</sup> in the ligand structure), but substantial transition integrals to an adjacent fragment (Fc) will occur, promoting lateral charge transfer rates within the interface layer. Calculating the electron transfer integral values  $V$  between neighboring sites is the first step in theoretically quantifying an electron hopping rate within the ligand layer using a Marcus electron transfer model. However, for such a model, these considerable reorganization energies must be calculated for a ligand structure in the layer. Alternatively, one might choose a solid-state polaron model,<sup>[84]</sup> although a more

chemical model with hopping between fragment units is desirable. For a simple fragment-based charge transfer analysis<sup>[85–87]</sup> within a model of two neighboring ferrocene ligands, a first DFT calculation using the ADF code on PBE and triple zeta level of theory<sup>[88]</sup> yielded a value of  $V_{\text{electron}} = 0.0064$  eV for the electron transfer integral ( $V_{\text{hole}}$  is negligible). Neglecting entropic contributions, one estimates an electron hopping rate of the order of  $k = 1 \times 10^{-10}$  s<sup>-1</sup> from Fe<sup>2+</sup> to Fe<sup>3+</sup> sites at  $T = 300$  K using the calculated reorganization energies of  $\lambda = 0.32$  eV within the Marcus model.

When a second perchlorate is adsorbed to the surface the charge becomes almost uniformly distributed over the Fe centers (Figure 6c). These calculations demonstrate nevertheless how the positive charge becomes nearly evenly distributed over all Fe centers for a 1:1 ratio of Fe<sup>3+</sup>/Fe<sup>2+</sup>. In our model, one would then have four sites and two electrons (holes). In reality, one would have to consider a large number  $N$  of sites and  $N/2$  electrons (ignoring spin) leading to a half-filled energy band shown schematically in Figure 6f (SOMO<sub>band</sub>). In our simplistic model, the transfer integrals for all pairs of Fe-sites will contribute to the width of this band.

This positive charge can evenly polarize the ligand-layer/semiconductor ribbon interface and might change the semiconducting properties as found in the experiments, especially if excited electrons will be involved. In an electron transfer picture, this means considerable transfer rates of electrons between several neighboring iron sites. Such an ensemble of electrons could be a model for the formation of the new SOMO band.

The Helmholtz layer model in Figure 6a–c can hence illustrate the ligand layer and allows electron hopping and delocalization to be discussed for the electronic ground state. A discussion of excited states with a strong coupling between the ligand layer and semiconducting [PbBr<sub>3</sub>]<sup>-</sup>-ribbons would be ideal to study the optical properties of the system and could clarify electron and hole transfer between ribbon and Helmholtz layer. However, accurate quantum chemical calculations of the band structure in these extended complex systems, are already very difficult.<sup>[84]</sup> For nonperiodic systems such as semiconductor clusters with single ligands, HOMO-LUMO gaps can in principle be calculated by using DFT with the GW method,<sup>[76]</sup> but a complete ligand layer would be a much more challenging task. Therefore, for now, one must rely on an initial qualitative discussion of the gap as in Figure 6, which is consistent with the experimental data.

We conclude that at low oxidation degrees local defect states are created, which result in radiative emission upon excitation of charge carriers in the semiconductor (Figure 6e). A charge carrier transfer from the electronic bands of the semiconducting lead bromide ribbons to the Fc<sup>+</sup>-ligands occurs, as the molecular orbitals lie favorable between the VBM and CBM. Accordingly, a higher degree of oxidation leads to delocalization of electrons over several ligands and electron hopping according to the Marcus theory (Figure 6f). Therefore, the formation of a novel electronic band SOMO<sub>band</sub> is observed. Electrons from this band can now be transferred into the CBM by optical excitation, which is why a narrowing of the bandgap is obtained. The new, indirect bandgap is now 3.27 eV, which is 0.24 eV smaller than for the unoxidized material.

### 3. Conclusion

Designing novel ligands for the synthesis of hybrid semiconductor materials is known to bear great potential, as it is possible to tailor electro-optical features. Ferrocene is not only interesting as a strongly structure-directing ligand, the oxidation also shows remarkable effects on the electronic situation in the semiconductor, as defect states in the bandgap define the electro-optical properties.

In the current work, three novel Fc-ligands with suitable head groups for the synthesis of hybrid lead bromide semiconductor particles were presented. The crystal structures of the resulting particles were determined by 3D ED and modeling. It is revealed that Coulombic attractions between the Fc-ligands as well as hydrogen bonds between the linking carboxyl group and the ammonium head group result in strong templating effects of the inorganic network. Therefore, the formation of more exotic inorganic structural motives from ribbons to 2D layered structures is observed. As the head group becomes longer, the interaction between the ester and the ammonium head group decreases, leading to weaker structure-directing properties of the Fc ligand. Thus, the Fc units can assemble more efficiently with increasing spacer length and, at the same time, the lead bromide phase is less constrained, leading to a decrease in density. Depending on the connectivity of the octahedra the bandgap decreases from 3.51 to 3.06 eV with increasing length of the head group. For Ruddlesden–Popper phases, thin film preparation is a well-known method for structure elucidation, which we want to investigate with (FcC<sub>6</sub>)<sub>2</sub>PbBr<sub>4</sub> in our future research. Furthermore, for the unambiguous structural elucidation of (FcC<sub>6</sub>)<sub>2</sub>PbBr<sub>4</sub>, we plan to use improved 3D ED techniques, which allow the investigations of very beam-sensitive materials.

Redox activity of the Fc-ligands in the material was proven by CV. Chemical oxidation was used to adjust the Fc<sup>+</sup>/Fc ratio and to observe alterations in optoelectronic properties. Depending on the degree of oxidation, the material showed the formation of radiative defect states, which at a high degree of oxidation even resulted in the formation of a new electronic band. Ab initio calculations using the BAND code of the oxidized structure showed that the paramagnetic spins of the unpaired electron of the oxidized Fe<sup>3+</sup>-cations are delocalized between the Fc-ligands and may “hop” between the Fe-central atoms. The lowest energy transition is thus no longer from the VBM to the CBM, but a transition from the new Fe<sup>3+</sup>-band to the CBM, which is by  $\Delta E = 0.24$  eV smaller than the initial bandgap. For a classical semiconductor, it is set, if it possesses an indirect gap (PL silent) or a direct gap which shows fluorescence. In ferrovskites one can switch between these two states, which is one aspect making the materials special.

Our results suggest that ligand design is crucial for the formed crystal structure and thus desired properties such as stability and bandgap of hybrid materials are highly tunable. Carboxyl groups have a great influence on the structure formation and could help to create tailor-made crystal structures with extraordinary properties. Also, the combination with a redox-active ligand offers a novel possibility to modify the optoelectronic properties of semiconductors. Furthermore, the successful oxidation of Fe<sup>2+</sup> now also makes it possible to

actively influence the magnetic properties of the semiconductors. The presence of a paramagnetic spin in the  $\text{Fe}^{3+}$  can lead to unusual effects in the magnetic field, so that these materials could become interesting in spintronics, for example. In the future, we want to focus on these investigations.

## 4. Experimental Section

**Chemicals:** Lead (II) bromide ( $\text{PbBr}_2$ , Sigma-Aldrich, 99.9% purity), methyl amine ( $\text{CH}_3\text{NH}_2 \cdot \text{H}_2\text{O}$ , Sigma Aldrich, 33 wt% in EtOH), hydrobromic acid (48 wt% in  $\text{H}_2\text{O}$ , Sigma-Aldrich), ferrocene carboxylic acid ( $\text{C}_{10}\text{H}_{11}\text{FeO}_2$ , Sigma-Aldrich, 96% purity), N-Boc ethanolamine ( $\text{C}_7\text{H}_{15}\text{NO}_3$ , Sigma Aldrich, 98% purity), 3-(Boc-amino)-1-propanol ( $\text{C}_8\text{H}_{17}\text{NO}_3$ , TCI Chemicals, 96% purity), 4-(Boc-amino)-1-butanol ( $\text{C}_9\text{H}_{19}\text{NO}_3$ , TCI Chemicals, 97% purity), 5-(Boc-amino)-1-pentanol ( $\text{C}_{10}\text{H}_{21}\text{NO}_3$ , TCI Chemicals, 97% purity), 6-(Boc-amino)-1-hexanol ( $\text{C}_{11}\text{H}_{23}\text{NO}_3$ , Sigma Aldrich, 98% purity), 4-(dimethylamino) pyridine (DMAP,  $\text{C}_7\text{H}_{10}\text{N}_2$ , Sigma Aldrich), N-(3-dimethylaminopropyl)-N'-ethylcarbodiimide hydrochloride (EDC-HCl,  $\text{C}_8\text{H}_{17}\text{N}_3 \cdot \text{HCl}$ , TCI Chemicals, 98% purity), trifluoroacetic acid (TFA,  $\text{C}_2\text{H}_3\text{O}_2\text{F}_3$ , Sigma Aldrich), hydrobromic acid (HBr, 48 wt% in  $\text{H}_2\text{O}$ , Sigma Aldrich), diethyl carbonate [DEC, ( $\text{C}_2\text{H}_5\text{O}$ ) $_2\text{CO}$ , Sigma Aldrich, 99% purity], bis(trifluoromethane)sulfonimide lithium salt (LiTFSI,  $\text{CF}_3\text{SO}_2\text{N}(\text{Li})\text{SO}_2\text{CF}_3$ , Sigma Aldrich), methoxyperfluorobutane (HFE-7100, Sigma Aldrich, 99% mixture of *n*- and *iso*-butyl isomers), and iron(III) perchlorate hydrate ( $\text{Fe}(\text{ClO}_4)_3 \cdot x\text{H}_2\text{O}$ , Sigma Aldrich).

**Synthesis of  $\text{Fc}_n\text{Br}$  ( $n = 2, 4, 6$ ):** Starting from ferrocene carboxylic acid, Boc-protected amino alcohols were coupled to the carboxyl group via an ester coupling. 2.2 mmol ferrocene carboxylic acid was dissolved in 50 mL DCM using ultrasound. Then 2.2 mmol of the Boc-protected amine, 2.6 mmol DMAP, and 2.6 mmol EDC-HCl were added to the mixture in this order. After addition of all reactants, any remaining solids should have dissolved. The mixture was then heated under reflux to 50 °C for 16 h overnight. The solvent was removed and the brown solid was filtered with ethyl acetate over  $\approx 4$  cm of silica gel to give a yellow solution. The solvent was removed, giving a yellow to orange solid (yield:  $\text{Fc}_2 = 95.5\%$ ,  $\text{Fc}_4 = 68.3\%$ ,  $\text{Fc}_6 = 76.3\%$ ).

To remove the Boc-protecting group, the solid was dissolved in DCM and deprotected with 30 eq TFA for 1 h at 50 °C under reflux. The solvent was removed, giving a yellow to orange product. The deprotection was quantitative and was checked by thin film chromatography.

All amines were further solved in 1,4-dioxane and treated with HBr (1.5 eq) to obtain the ammonium salt. The solvent was removed, the obtained brown solid was solved in sufficient EtOH and reprecipitated with diethyl ether ( $\text{Et}_2\text{O}$ ). The powder was filtrated, washed with  $\text{Et}_2\text{O}$  and dried under reduced pressure. All products were characterized with  $^1\text{H-NMR}$ ,  $^{13}\text{C-NMR}$  (see Figures S1-S2, Supporting Information) and ESI-MS and further used for the material synthesis.

$^1\text{H-NMR}$  (400 MHz, DMSO- $d_6$ )  $n = 2$ :  $\delta$  (ppm) = 7.95 (s, 3H,  $\text{NH}_3$ ), 4.87 (t, 2H, CH), 4.50 (t, 2H, CH), 4.29 (t, 2H,  $\text{CH}_2$ ), 4.23 (s, 5H, cp-ring), 3.16 (t, 2H,  $\text{CH}_2$ );  $n = 4$ :  $\delta$  (ppm) = 4.73 (t, 2H, CH), 4.48 (t, 2H, CH), 4.22 (s, 5H, cp-ring), 4.16 (t, 2H,  $\text{CH}_2$ ), 2.85 (s, 2H,  $\text{CH}_2$ ), 1.69 (m, 4H,  $\text{CH}_2$ );  $n = 6$ :  $\delta$  (ppm) = 4.72 (t, 2H, CH), 4.47 (t, 2H, CH), 4.20 (s, 5H, cp-ring), 4.14 (t, 2H,  $\text{CH}_2$ ), 2.78 (s, 2H,  $\text{CH}_2$ ), 1.64 (p, 2H,  $\text{CH}_2$ ), 1.55 (m, 2H,  $\text{CH}_2$ ), 1.39 (m, 6H,  $\text{CH}_2$ )

$^{13}\text{C-NMR}$  (400 MHz, DMSO- $d_6$ )  $n = 2$   $\delta$  (ppm) = 170.14 (O=C-O), 71.09 (2C, CH-cp), 69.68 (CH $_2$ ) 69.66 (2C, CH-cp) 69.27 (5C, CH-cp), 65.93 (CH $_2$ );  $n = 4$   $\delta$  (ppm) = 170.08 (O=C-O), 70.85 (2C, CH-cp), 70.27 (1C, CH-cp) 69.19 (2C, CH-cp), 69.07 (5C, CH-cp), 62.61 (CH $_2$ ), 38.04 (CH $_2$ ), 24.93 (CH $_2$ ), 23.35 (CH $_2$ );  $n = 6$   $\delta$  (ppm) = 170.04 (O=C-O), 70.78 (2C, CH-cp), 70.40 (1C, CH-cp), 69.14 (2C, CH-cp), 68.97 (5C, CH-cp), 62.63 (CH $_2$ ), 39.73 (CH $_2$ ), 27.65 (CH $_2$ ), 24.44 (CH $_2$ ).

ESI-MS of  $n = 2$  Expected 275.05 Observed 275.13;  $n = 4$  Expected 302.08 Observed 302.20;  $n = 6$  Expected 331.12 Observed 331.16.

**Synthesis of  $(\text{FcC}_2)\text{PbBr}_3$  Phase:** For the material synthesis of  $(\text{FcC}_2)\text{PbBr}_3$  a precursor solution with a concentration of 0.1 M in DMF

was produced. 1 eq of  $\text{PbBr}_2$  and 1 eq of  $\text{FcC}_2\text{Br}$  were dissolved in dried DMF. Under vigorous stirring 0.2 mL of the precursor solution was added quickly into 30 mL DCM. The suspension was stirred for 1 h, then the precipitation was centrifuged, washed three times with 3 mL DCM and dried under reduced pressure. The samples were kept under nitrogen atmosphere to prevent decomposition.

**Synthesis of  $(\text{FcC}_4)_4\text{Pb}_3\text{Br}_{10}$  Phase:** For the material synthesis of  $(\text{FcC}_4)_4\text{Pb}_3\text{Br}_{10}$  a precursor solution with a concentration of 0.1 M in DMF was produced. Therefore, 3 eq of  $\text{PbBr}_2$  and 4 eq of  $\text{FcC}_4\text{Br}$  were dissolved in dried DMF. Under vigorous stirring 0.2 mL of the precursor solution was added quickly into 30 mL DCM. The suspension was stirred for 1 h, then the precipitation was centrifuged, washed three times with 3 mL DCM and dried under reduced pressure. The sample was kept under nitrogen atmosphere to prevent decomposition.

**Synthesis of  $(\text{FcC}_6)_2\text{PbBr}_4$  Phases:** For the material synthesis of  $(\text{FcC}_6)_2\text{PbBr}_4$  a precursor solution with a concentration of 0.1 M in DMF was produced. Therefore, 1 eq of  $\text{PbBr}_2$  and 2 eq of  $\text{FcC}_6\text{Br}$  were dissolved in dried DMF. Under vigorous stirring 0.2 mL of the precursor solution was added quickly into 30 mL toluene. The suspension was stirred for 1 h, then the precipitation was centrifuged, washed three times with 3 mL DCM and dried under reduced pressure. The sample was kept under nitrogen atmosphere to prevent decomposition.

**Oxidation of  $(\text{FcC}_2)\text{PbBr}_3$  with Iron(III) Perchlorate Hydrate:** For the chemical oxidation of the  $(\text{FcC}_2)\text{PbBr}_3$  particles, iron (III) perchlorate ( $\text{Fe}(\text{ClO}_4)_3$ ) was dried for 24 h at 60 °C under reduced pressure. A stock solution of  $\text{Fe}(\text{ClO}_4)_3$  in  $\text{CHCl}_3$  ( $10^{-3}$  M) was prepared. 1 mg of  $(\text{FcC}_2)\text{PbBr}_3$  (1.4  $\mu\text{mol}$ ) were dispersed in 3 mL diluted solution of  $\text{Fe}(\text{ClO}_4)_3$  with varying equivalents (0.1, 0.2, 0.5, 1.0, and 2.0 eq) of oxidant and treated with ultrasound for 10 min. The particles were centrifuged, washed three times with 3 mL  $\text{CHCl}_3$  and dried under reduced pressure. SEM images of the oxidized particles are provided in Figure S17 (Supporting Information). The samples were kept under nitrogen atmosphere to prevent decomposition.

**Cyclic Voltammetry Measurements:** For CV measurements, 1.44 g LiTFSI (5 mmol; salt was stored in a glovebox) were solved in 48.5 mL HFE and 1.5 mL DEC. To remove dissolved oxygen, the solution was flushed with nitrogen for 10 min. ITO substrates were ultrasonically cleaned in a soap solution, ethanol and then acetone, 20 min each. The substrates were dried under a  $\text{N}_2$  stream. The coated ITO substrate was prepared by drop-casting a concentrated dispersion of the particles in toluene onto an area of about 1 cm  $\times$  1 cm. The solvent was evaporated on a heat-plate at 40 °C. The counter electrode, a Pt-plate, was cleaned in  $\text{H}_2\text{SO}_4/\text{H}_2\text{O}_2$ , washed with deionized water, ethanol and acetone. Before use, the Pt plate was dried under a  $\text{N}_2$  stream. For the measurement, all electrodes were contacted with alligator clips and the electrodes were immersed in 30 mL of the electrolyte in a beaker. For oxidation experiments (30 min at 0.65 V) the electrolyte was slightly stirred.

**3D Electron Diffraction:** All measurements of  $(\text{FcC}_2)\text{PbBr}_3$  and  $(\text{FcC}_4)_4\text{Pb}_3\text{Br}_{10}$  were carried out with a TEM FEI Tecnai F30 S-TWIN equipped with a field emission gun (300 kV) or with a TEM FEI Tecnai 20 equipped with a LaB6 cathode (200 kV), respectively. The powdered sample was dispersed in ethanol using an ultrasonic bath and sprayed on carbon-coated copper grid using an ultrasound sonifier.<sup>[43]</sup> Measurements for  $(\text{FcC}_2)\text{PbBr}_3$  were carried out with the FEI Tecnai F30, TEM images and ED patterns were acquired with a Gatan UltraScan4000 CCD camera (16-bit, 4096  $\times$  4096 pixel) at hardware-binning of 4. Scanning transmission electron microscopy (STEM) images were collected by a FISCHIONE high-angular annular dark field (HAADF) detector and acquired by Emisspec ES Vision software. 3D ED data were collected using the acquisition module Fast-ADT (FADT)<sup>[45]</sup> developed for FEI and JEOL microscopes. A condenser aperture of 10  $\mu\text{m}$  and mild illumination settings (gun lens 8, spot size 6) were used to produce a semi-parallel beam of 550 nm in diameter ( $0.090 \text{ e}^- \text{ \AA}^{-2} \text{ s}^{-1}$ ). Crystal position tracking was performed in microprobe STEM mode. In case of  $(\text{FcC}_4)_4\text{Pb}_3\text{Br}_{10}$  measurements were performed with the FEI Tecnai 20, TEM images and ED patterns were recorded using a single-electron ASI MEDIPIX detector<sup>[89]</sup> (16-bit, 512  $\times$  512 pixel). Mild illumination settings were used (condenser aperture of 10  $\mu\text{m}$  and spot size 8) to produce a semiparallel beam of 1050 nm



in diameter ( $0.060 \text{ e}^- \text{ \AA}^{-2} \text{ s}^{-1}$ ). 3D ED data were collected using the authors' own developed scripts in Olympus Soft Imaging Solutions iTEM software. The ED data were collected on both TEMs with electron beam precession (precession electron diffraction, PED) to improve reflection intensity integration quality.<sup>[43,90]</sup> PED was performed using a Digistar unit developed by NanoMEGAS SPRL. The precession angle was kept at  $\approx 1^\circ$ . The PETS2.0 software package<sup>[91]</sup> was used for 3D ED data processing. Difference Fourier mapping and least-squares (dynamical) refinement were performed with the software JANA2006.<sup>[92]</sup>

**Powder X-Ray Diffraction:** Measurements of the particles were obtained using an X-ray diffractometer with Debye–Scherrer setup (StadiP by Stoe) using monochromatic  $\text{CuK}\alpha_1$  radiation ( $\lambda = 1.54059 \text{ \AA}$ ). The diffractometer was equipped with a Mythen 1K detector (Dectris) with an angular range of  $12.5^\circ$ . PXRD measurements of drop-casted particles on ITO substrate were obtained using an X-ray diffractometer with Bragg–Brentano setup (ThetaTheta by Stoe) using  $\text{CuK}\alpha_1$  radiation ( $\lambda = 1.54059 \text{ \AA}$ ).

**Other Characterization:** SEM images and energy-dispersive X-ray (EDX) spectroscopy of drop-casted particles on silicon substrate were obtained using a Jeol JSM-6700F equipped with an Oxford Instruments INCA 300. UV–vis measurements of drop-casted particles on ITO substrate were acquired with an Agilent 8453 Carry 4000 with a praying mantis. UV–vis measurements of drop-casted particles on glass substrate were acquired with an Agilent 8453 Carry 5000 with an integrating sphere. For evaluation of the bandgap the Kubelka–Munk method was used. UV–vis measurements of particles in dispersion and the  $\text{FcC}_n\text{Br}$ -ligands ( $n = 2, 4, 6$ ) in solution were obtained with an Agilent 8453 Carry 4000. Photon electron spectroscopy (on air; PESA) of drop-casted particles on a glass substrate were acquired with a Riken Keiki AC-2 Photoelectron Spectrometer. XPS measurements were obtained with a Versaprobe III (Physical Electronics GmbH). PL measurements of particles suspended in toluene were obtained using a Cary Eclipse (Agilent). Cyclic voltammetry measurements were obtained with a potentiostat (Autolab, PGSTAT101) from Metrohm.

**Statistical Analysis:** A descriptive statistical analysis was not subject of this research.

1. Preprocessing of data: For representation of UV–vis reflectance, UV–vis absorption, XPS, PXRD, and PL emission, data were normalized to 1.
2. Data presentation: No statistical analysis was obtained. Particles from the same batch were used for all investigations.
3. Sample size: Particles from the same batch were used for all investigations.
4. Statistical methods used: No statistical analysis was performed with the presented samples.
5. Software used for statistical analysis: Data plotting, fitting, and normalization were performed using OriginPro 2021.

## Supporting Information

Supporting Information is available from the Wiley Online Library or from the author.

## Acknowledgements

The authors thank the German Research Foundation for funding (project PO 780/22-1). The authors thank Ute Kolb for access to the transmission electron microscope FEI Tecnai F30 S-TWIN at the EM Center in Mainz (EZMZ) of the university Mainz. The authors are grateful to Lukáš Palatinus for access to the TEM FEI Tecnai 20 at the Institute of Physics of the Czech Academy of Sciences. The authors thank Stefan Schupp for organizing the PESA measurements and Stephen Klimke for the Mößbauer analysis. The authors thank the LNQE Research Center for the use of the XPS.

Open access funding enabled and organized by Projekt DEAL.

## Conflict of Interest

The authors declare no conflict of interest.

## Data Availability Statement

The data that support the findings of this study are available in the Supporting Information of this article.

## Keywords

ferrocene materials, hybrid perovskites, MicroED, molecular switches, semiconductors

Received: January 27, 2022

Revised: February 23, 2022

Published online: March 8, 2022

- [1] Y. Sun, J. A. Rogers, *Adv. Mater.* **2007**, *19*, 1897.
- [2] S. K. Garlapati, M. Divya, B. Breitung, R. Kruk, H. Hahn, S. Dasgupta, *Adv. Mater.* **2018**, *30*, 1707600.
- [3] D. B. Mitzi, *J. Mater. Chem.* **2004**, *14*, 2355.
- [4] H. J. Snaith, *J. Phys. Chem. Lett.* **2013**, *4*, 3623.
- [5] N. Pellet, F. Giordano, M. I. Dar, G. Gregori, S. M. Zakeeruddin, J. Maier, M. Grätzel, *Prog. Photovolt. Res. Appl.* **2017**, *25*, 942.
- [6] T. C. Sum, N. Mathews, G. Xing, S. S. Lim, W. K. Chong, D. Giovanni, H. A. Dewi, *Acc. Chem. Res.* **2016**, *49*, 294.
- [7] J. S. Manser, J. A. Christians, P. V. Kamat, *Chem. Rev.* **2016**, *116*, 12956.
- [8] A. Amat, E. Mosconi, E. Ronca, C. Quarti, P. Umari, M. d. K. Nazeeruddin, M. Grätzel, F. De Angelis, *Nano Lett.* **2014**, *14*, 3608.
- [9] M. R. Filip, G. E. Eperon, H. J. Snaith, F. Giustino, *Nat. Commun.* **2014**, *5*, 5757.
- [10] S. Gonzalez-Carrero, R. E. Galian, J. Pérez-Prieto, *J. Mater. Chem. A* **2015**, *3*, 9187.
- [11] Y. Zhao, K. Zhu, *Chem. Soc. Rev.* **2016**, *45*, 655.
- [12] A. L. Abdelhady, M. I. Saidaminov, B. Murali, V. Adinolfi, O. Voznyy, K. Katsiev, E. Alarousu, R. Comin, I. Dursun, L. Sinatra, E. H. Sargent, O. F. Mohammed, O. M. Bakr, *J. Phys. Chem. Lett.* **2016**, *7*, 295.
- [13] D. M. Jang, K. Park, D. H. Kim, J. Park, F. Shojaei, H. S. Kang, J. P. Ahn, J. W. Lee, J. K. Song, *Nano Lett.* **2015**, *15*, 5191.
- [14] S. Ji, X. Yuan, S. Cao, W. Ji, H. Zhang, Y. Wang, H. Li, J. Zhao, B. Zou, *J. Phys. Chem. Lett.* **2020**, *11*, 2142.
- [15] R. Begum, M. R. Parida, A. L. Abdelhady, B. Murali, N. M. Alyami, G. H. Ahmed, M. N. Hedhili, O. M. Bakr, O. F. Mohammed, *J. Am. Chem. Soc.* **2017**, *139*, 731.
- [16] G. Grancini, C. Roldan-Carmona, I. Zimmermann, E. Mosconi, X. Lee, D. Martineau, S. Narbey, F. Oswald, F. De Angelis, M. Graetzel, M. K. Nazeeruddin, *Nat. Commun.* **2017**, *8*, 15684.
- [17] H. Tsai, W. Nie, J. C. Blancon, C. C. Stoumpos, R. Asadpour, B. Harutyunyan, A. J. Neukirch, R. Verduzco, J. J. Crochet, S. Tretiak, L. Pedesseau, J. Even, M. A. Alam, G. Gupta, J. Lou, P. M. Ajayan, M. J. Bedzyk, M. G. Kanatzidis, *Nature* **2016**, *536*, 312.
- [18] E. R. Dohner, A. Jaffe, L. R. Bradshaw, H. I. Karunadasa, *J. Am. Chem. Soc.* **2014**, *136*, 13154.
- [19] L. Mao, P. Guo, M. Kepenekian, I. Hadar, C. Katan, J. Even, R. D. Schaller, C. C. Stoumpos, M. G. Kanatzidis, *J. Am. Chem. Soc.* **2018**, *140*, 13078.

- [20] M. D. Smith, B. A. Connor, H. I. Karunadasa, *Chem. Rev.* **2019**, *119*, 3104.
- [21] G.-E. Wang, C. Sun, M.-S. Wang, G.-C. Guo, *Nanoscale* **2020**, *12*, 4771.
- [22] T. Kong, H. Xie, Y. Zhang, J. Song, Y. Li, E. L. Lim, A. Hagfeldt, D. Bi, *Adv. Energy Mater.* **2021**, *11*, 2101018.
- [23] F. Xu, Y. Li, N. Liu, Y. Han, M. Zou, T. Song, *Crystals* **2021**, *11*, 241.
- [24] Y. Miao, X. Wang, H. Zhang, T. Zhang, N. Wei, X. Liu, Y. Chen, J. Chen, Y. Zhao, *eScience* **2021**, *1*, 91.
- [25] A. F. Xu, R. T. Wang, L. W. Yang, V. Jarvis, J. F. Britten, G. Xu, *Chem. Commun.* **2019**, *55*, 3251.
- [26] C. Elliott, J. A. McNulty, D. B. Cordes, A. M. Z. Slawin, P. Lightfoot, *J. Solid State Chem.* **2021**, *303*, 122466.
- [27] X. Li, Y. He, M. Kepenekian, P. Guo, W. Ke, J. Even, C. Katan, C. C. Stoumpos, R. D. Schaller, M. G. Kanatzidis, *J. Am. Chem. Soc.* **2020**, *142*, 6625.
- [28] P. Kour, M. Chenna Reddy, S. Pal, S. Sidhik, T. Das, P. Pandey, S. P. Mukherjee, S. Chakraborty, A. D. Mohite, S. Ogale, *Angew. Chem., Int. Ed.* **2021**, *60*, 18750.
- [29] C. C. Stoumpos, L. Mao, C. D. Malliakas, M. G. Kanatzidis, *Inorg. Chem.* **2017**, *56*, 56.
- [30] D. B. Mitzi, K. Chondroudis, C. R. Kagan, *ACS Inorg. Chem.* **1999**, *38*, 11.
- [31] J. V. Milić, *J. Mater. Chem. C* **2021**, 11428.
- [32] J. V. Passarelli, D. J. Fairfield, N. A. Sather, M. P. Hendricks, H. Sai, C. L. Stern, S. I. Stupp, *J. Am. Chem. Soc.* **2018**, *140*, 7313.
- [33] W. Chen, Y. Shi, J. Chen, P. Ma, Z. Fang, D. Ye, Y. Lu, Y. Yuan, J. Zhao, Z. Xiao, *Adv. Mater.* **2021**, *33*, 2104842.
- [34] N. Fillafer, T. Seewald, L. Schmidt-Mende, S. Polarz, *Beilstein J. Nanotechnol.* **2020**, *11*, 466.
- [35] Z.-X. Zhang, H.-Y. Zhang, W. Zhang, X.-G. Chen, H. Wang, R.-G. Xiong, *J. Am. Chem. Soc.* **2020**, *142*, 17787.
- [36] D. Astruc, *Eur. J. Inorg. Chem.* **2017**, 2017, 6.
- [37] Z. Huang, H. Yu, L. Wang, X. Liu, T. Lin, F. Haq, S. Z. Vatsadze, D. A. Lemenovskiy, *Coord. Chem. Rev.* **2021**, *430*, 213737.
- [38] G. S. Mohammad-Pour, K. O. Hatfield, D. C. Fairchild, K. Hernandez-Burgos, J. Rodríguez-López, F. J. Uribe-Romo, *J. Am. Chem. Soc.* **2019**, *141*, 19978.
- [39] L. Fabbrizzi, *ChemTexts* **2020**, *6*, 22.
- [40] M. Gemmi, E. Mugnaioli, T. E. Gorelik, U. Kolb, L. Palatinus, P. Boullay, S. Hovmöller, J. P. Abrahams, *ACS Cent. Sci.* **2019**, *5*, 1315.
- [41] Y. Krysiak, M. Maslyk, B. N. Silva, S. Plana-Ruiz, H. M. Moura, E. O. Munsignatti, V. S. Vaiss, U. Kolb, W. Tremel, L. Palatinus, *Chem. Mater.* **2021**, *33*, 3207.
- [42] X. Feng, M. Tan, M. Li, H. Wei, B. Yang, *Nano Lett.* **2021**, *21*, 1500.
- [43] E. Mugnaioli, T. Gorelik, U. Kolb, *Ultramicroscopy* **2009**, *109*, 758.
- [44] U. Kolb, Y. Krysiak, S. Plana-Ruiz, *Acta Crystallogr., B* **2019**, *75*, 463.
- [45] S. Plana-Ruiz, Y. Krysiak, J. Portillo, E. Alig, S. Estradé, F. Peiró, U. Kolb, *Ultramicroscopy* **2020**, *211*, 112951.
- [46] L. Palatinus, P. Brázda, P. Boullay, O. Perez, M. Klementová, S. Petit, V. Eigner, M. Zaarour, S. Mintova, *Science* **2017**, *355*, 166.
- [47] D. Bowden, Y. Krysiak, L. Palatinus, D. Tsivoulas, S. Plana-Ruiz, E. Sarakinou, U. Kolb, D. Stewart, M. Preuss, *Nat. Commun.* **2018**, *9*, 1374.
- [48] P. Brázda, L. Palatinus, M. Babor, *Science* **2019**, *364*, 667.
- [49] P. Klar, Y. Krysiak, H. Xu, G. Steciuk, J. Cho, X. Zou, L. Palatinus, **2021**.
- [50] J. Simancas, R. Simancas, P. J. Bereciartua, J. L. Jorda, F. Rey, A. Corma, S. Nicolopoulos, P. P. Das, M. Gemmi, E. Mugnaioli, *J. Am. Chem. Soc.* **2016**, *138*, 10116.
- [51] E. Mugnaioli, A. E. Lanza, G. Bortolozzi, L. Righi, M. Merlini, V. Cappello, L. Marini, A. Athanassiou, M. Gemmi, *ACS Cent. Sci.* **2020**, *6*, 1578.
- [52] Y. Krysiak, B. Marler, B. Barton, S. Plana-Ruiz, H. Gies, R. B. Neder, U. Kolb, *IUCrj* **2020**, *7*, 522.
- [53] M. J. de la Cruz, J. Hattne, D. Shi, P. Seidler, J. Rodriguez, F. E. Reyes, M. R. Sawaya, D. Cascio, S. C. Weiss, S. K. Kim, *Nat. Methods* **2017**, *14*, 399.
- [54] J. Hattne, M. W. Martynowycz, P. A. Penczek, T. Gonen, *IUCrj* **2019**, *6*, 921.
- [55] C. M. Gillavry, H. Nijveld, S. Dierdorp, J. Karsten, *Rec. Trav. Chim. Pays Bas* **1939**, *58*, 193.
- [56] C. P. Brock, Y. Fu, *Acta Crystallogr., B* **1997**, *53*, 928.
- [57] H. Steinfink, G. D. Brunton, *Inorg. Chem.* **1969**, *8*, 1665.
- [58] T. Wiest, R. Blachnik, H. Reuter, *Z. Naturforsch.* **1999**, *54 b*, 1099.
- [59] M. D. Smith, B. L. Watson, R. H. Dauskardt, H. I. Karunadasa, *Chem. Mater.* **2017**, *29*, 7083.
- [60] B. Saparov, D. B. Mitzi, *Chem. Rev.* **2016**, *39*.
- [61] N. Kitazawa, *Mater. Sci. Eng., B* **1997**, *49*, 233.
- [62] A. Paul, R. Borrelli, H. Bouyanfif, S. Gottis, F. Sauvage, *ACS Omega* **2019**, *4*, 14780.
- [63] M. D. Smith, H. I. Karunadasa, *Acc. Chem. Res.* **2018**, *51*, 619.
- [64] Z. Yuan, C. Zhou, Y. Tian, Y. Shu, J. Messier, J. C. Wang, L. J. van de Burgt, K. Kountouriotis, Y. Xin, E. Holt, K. Schanze, R. Clark, T. Siegrist, B. Ma, *Nat. Commun.* **2017**, *8*, 14051.
- [65] S. Fery-Forgues, B. Delavaux-Nicot, *J. Photochem. Photobiol.* **2000**, *132*, 137.
- [66] M. Hasan, S. Venkatesan, D. Lyashenko, J. D. Slinker, A. Zakhidov, *Anal. Chem.* **2017**, *89*, 9649.
- [67] N. G. Tsierkezos, *J. Solut. Chem.* **2007**, *36*, 289.
- [68] R. H. Palmer, J. Liu, C.-W. Kung, I. Hod, O. K. Farha, J. T. Hupp, *Langmuir* **2018**, *34*, 4707.
- [69] R. Prins, *J. Chem. Soc. D* **1970**, 280b.
- [70] M. Rowe, A. McCaffery, *J. Chem. Phys.* **1973**, *59*, 3786.
- [71] K.-F. Berggren, B. E. Sernelius, *Phys. Rev. B* **1981**, *24*, 1971.
- [72] V. Palankovski, G. Kaiblinger-Grujin, S. Selberherr, *Mater. Sci. Eng., B* **1999**, *66*, 46.
- [73] G. Philippen, G. te Velde, E. J. Baerends, J. A. Berger, P. L. de Boeij, M. Franchini, J. A. Groeneveld, E. S. Kadantsev, R. Klooster, F. Kootstra, M. C. W. M. Pols, P. Romaniello, M. Raupach, D. G. Skachkov, J. G. Snijders, C. J. O. Verzijl, J. A. Celis Gil, J. M. Thijssen, C. A. Peeples, G. Schreckenbach, T. Ziegler, *BAND 2021.1, SCM*, <http://www.scm.com> (accessed: December 2021).
- [74] C. Stangel, C. Schubert, S. Kuhri, G. Rotas, J. T. Margraf, E. Regulska, T. Clark, T. Torres, N. Tagmatarchis, A. G. Coutsolelos, *Nanoscale* **2015**, *7*, 2597.
- [75] R. E. Ruther, Q. Cui, R. J. Hamers, *J. Am. Chem. Soc.* **2013**, *135*, 5751.
- [76] K. Tarafder, Y. Surendranath, J. H. Olshansky, A. P. Alivisatos, L.-W. Wang, *J. Am. Chem. Soc.* **2014**, *136*, 5121.
- [77] R. A. Marcus, *Rev. Mod. Phys.* **1993**, *65*, 599.
- [78] J. O'M Bockris, M. GamboaAldeco, *Mod. Electrochem.* **2002**.
- [79] G. Te Velde, E. Baerends, *Phys. Rev. B* **1991**, *44*, 7888.
- [80] J. P. Perdew, K. Burke, M. Ernzerhof, *Phys. Rev. Lett.* **1996**, *77*, 3865.
- [81] F. L. Hirshfeld, *Theor. Chim. Acta* **1977**, *44*, 129.
- [82] K. B. Wiberg, P. R. Rablen, *J. Comput. Chem.* **1993**, *14*, 1504.
- [83] A. V. Marenich, S. V. Jerome, C. J. Cramer, D. G. Truhlar, *J. Chem. Theory Comput.* **2012**, *8*, 527.
- [84] E. Welch, L. Scolfaro, A. Zakhidov, *AIP Adv.* **2016**, *6*, 125037.
- [85] K. Senthilkumar, F. Grozema, F. Bickelhaupt, L. Siebbeles, *J. Chem. Phys.* **2003**, *119*, 9809.
- [86] K. Senthilkumar, F. C. Grozema, C. F. Guerra, F. M. Bickelhaupt, F. D. Lewis, Y. A. Berlin, M. A. Ratner, L. D. Siebbeles, *J. Am. Chem. Soc.* **2005**, *127*, 14894.
- [87] S.-H. Wen, A. Li, J. Song, W.-Q. Deng, K.-L. Han, W. A. Goddard III, *J. Phys. Chem. B* **2009**, *113*, 8813.
- [88] G. Te Velde, F. M. Bickelhaupt, E. J. Baerends, C. Fonseca Guerra, S. J. van Gisbergen, J. G. Snijders, T. Ziegler, *J. Comput. Chem.* **2001**, *22*, 931.
- [89] D. Georgieva, J. Jansen, I. Sikharulidze, L. Jiang, H. Zandbergen, J. Abrahams, *J. Instrum.* **2011**, *6*, C01033.
- [90] R. Vincent, P. Midgley, *Ultramicroscopy* **1994**, *53*, 271.
- [91] L. Palatinus, P. Brázda, M. Jelínek, J. Hrdá, G. Steciuk, M. Klementová, *Acta Crystallogr., B* **2019**, *75*, 512.
- [92] V. Petříček, M. Dušek, L. Palatinus, *Z. Kristallogr. Cryst. Mater.* **2014**, *229*, 345.